Silicon Electrolyte Interface Stabilization (SEISta)

Quarter 2 Report, FY20

Anthony Burrell
National Renewable Energy Laboratory
15013 Denver West Parkway
Golden, CO 80401
Phone: (303) 384-6666
E-mail: anthony.burrell@nrel.gov

Brian Cunningham, DOE-EERE-VTO Program Manager
Hybrid Electric Systems, Battery R&D
Phone: (202) 586-8055
E-mail: brian.cunningham@ee.doe.gov

Table of Contents

Page

Overview 1
Part 1: Understanding the Thermal Evolution of the SEI....5
Glyme-Based Electrolytes on a-Silicon Thin-Film Anodes: Surface Chemistry Evaluation....5
Localized Lithiation of Si with ≥ 5 nm Surface Thermal SiO_2 (NREL) 8
Part 2: Understanding Zintl Phase Stabilization of the SEI 12
Mechanistic Understanding of Zintl Phase in the SEI Using Model Systems 12
Part 3: Understanding Silicon Alloys Effect on the SEI 23
Silicon-Tin Alloys 23
Next-Generation Anodes for Lithium-Ion Batteries....31
Part 4: Influence of Carbon Dioxide on Si Anode Cycling....35

Project Introduction

This report documents the Silicon Electrolyte Interface Stabilization team's approach in 1) characterizing the early-stage silicon solid-electrolyte interphase (SEI) including progress on identifying the specific reaction pathways present in the formation of the SEI layer, and 2) establishing a procedure for measuring SEI growth rate at fixed potentials and different cycling regimes.

Silicon is a viable alternative to graphitic carbon as an electrode in lithium-ion cells and can theoretically store >3,500 mAh/g. However, lifetime problems have been observed that severely limit its use in practical systems. The major issues appear to involve the stability of the electrolyte and the uncertainty associated with the formation of a stable SEI at the electrode. Recently, calendar-life studies have indicated that the SEI may not be stable even under conditions where the cell is supposedly static. Clearly, a more foundational understanding of the nature of the silicon/electrolyte interface is required if we are to solve these complex stability issues. A

new multi-lab consortium has been formed to address a critical barrier in implementing a new class of materials used in lithium-ion batteries that will allow for smaller, cheaper, and better-performing batteries for electric-drive vehicles. This consortium, named the Silicon Electrolyte Interface Stabilization (SEISta) project, was formed to focus on overcoming the barrier to using such anode materials. Five national laboratories are involved: the National Renewable Energy Laboratory (NREL), Argonne National Laboratory (ANL), Lawrence Berkeley National Laboratory (LBNL), Oak Ridge National Laboratory (ORNL), and Sandia National Laboratories (SNL).

The SEISta project was specifically developed to tackle the foundational understanding of the formation and evolution of the solid-electrolyte interphase on silicon. This project will have as its primary goal an understanding of the reactivity of the silicon and lithiated silicon interface with the electrolyte in lithium-ion systems. It consists of researchers from NREL, ANL, LBNL, ORNL, and SNL working toward clear unified goals. The Silicon Deep-Dive team, which focuses on the science and technology barriers in functional electrodes, is a critical partner in this work. Many of the researchers are shared between both teams, and we hold joint meetings to ensure effective communication between the teams.

The current goals of SEISta are:

1. Have demonstrated ability to make model electrodes of Mg-Si Zintl compounds and compared SEI chemistry to silicon using XPS, STEM-EDS, and FTIR/Raman. **Q1 (100% Complete)**

2. Have established experiments and protocols for understanding the factors that affect safety in silicon anodes, with a specific focus on highly exothermic reactions that occur at silicon electrodes. **Q1 (100% Complete)**

3. Have determined the affect that CO_2 has on the stability of SEI formation on model electrodes, but examining the changes in the nature of the SEI (XPS, FTIR/Raman, and quantitative electrochemical measurement) as a function of CO_2 concentration. **Q2 (100% Complete)**

4. Have determined Zintl phase formation mechanism and its effect on SEI with model systems including Si nanoparticles, Si wafer, a-Si thin film using XPS, AFM/SSRM, STEM-EDS, and FTIR/Raman. **Q2 (100% Complete)**

5. Go/NoGo on production of tin-silicon alloys to be determined by the ability of the alloys to be prepared in 1-gram quantities and a demonstration that the alloys exhibit greater cyclic life than the pure metals alone. **Q2 (100% Complete, Decision = GO)**

6. Have determined the chemistry and interfacial properties (e.g., nature of the chemical bonding at the surface of Si and the organic material) of LiPAA/Si interfaces as a function of charge (OCV, 0.8 V, 0.4 V, 0.15 V, 0.05 V) and drying temperature (100, 125, 150, 175, 200 °C). **Q3**

7. Have determined how binder changes the stress/strain on silicon electrodes as a function of state of charge by varying Si nanoparticle size and surface functionally using both two- or three-dimensional model systems. **Q3**

8. Have implemented protocols that enable comparisons of safety responses in silicon anodes as a metric for improving safety in silicon cells. **Q3**

9. Have published a document that will enable other research and development groups to analyze stability of the SEI on a silicon-based anode, thus enabling developers or researchers to continually improve silicon cell stability (joint milestone with the Silicon Deep-Dive team). **Q4**

10. Have understood how the nature and amount of formed/soluble SEI species varies with electrolyte, binder, and Si anode (with surface functionalization) using GC-MS, (*in-situ*) FTIR/Raman, and XPS. **Q4**

Approach

The SEISta team works to ensure that protocols for sample preparation, experimental design, and implementation as well as data reporting are consistent across the whole team. Each laboratory is working toward the same set of quarterly milestones using its own specific talents and capabilities in a concerted effort with the other team members. This joint focus results in multiple researchers interacting to produce and analyze data to ensure that individual experimental variations will not lead to erroneous results. Critical to the success of this effort is the use of standard samples that can be shared by all parties. In addition to weekly whole-team video presentations, we have held on-site face-to-face meetings each quarter for all team members and other interested parties to brainstorm and sort out issues with existing experiments and jointly develop new experimental plans.

Objectives

The critical issues that SEISta is attempting to address are:

What are the properties of the lithiated silicon/electrolyte interface?

What is the silicon SEI actually made of and what reactions are contributing to it?

How fast does the silicon SEI grow?

Does it stop growing?

Is it soluble?

Can it be stabilized?

For FY20, the team continues to focus on three broad tasks:

Materials Standardization—This task is critical to developing and deploying standardized samples and experimental procedures across the team. We will continue to provide full characterization to any new sample that is to be used for SEI studies to ensure reproducibility and full understanding of the material. This quarter's work focused on developing new oxide coatings and methods to control the thickness and density of oxide samples. In addition, work on the silicon nanoparticles has made progress with the enhancement of the materials collection and handling system in the plasma reactor. *Although this work dominated the early part of the project and is still critical to its success, it is now only a minor part of the work, and this is reflected in the relative balance of this quarterly report.*

Model Materials Development and Characterization—The nature of the electrode-electrolyte interaction in silicon electrodes is at the heart of the formation and stability of the SEI. The synthesis of well-defined silicon nanoparticles and the different chemical markups of lithiated silicon surfaces is being probed by preparing model compounds and thin films that may/can exist in silicon anodes. Lithium silicides, silicates, and other inorganic material (LiF, Li_2O) are being prepared, and their reactivity with electrolytes is being determined. These materials also act as standard spectroscopy samples for the researchers who are looking at the formation of the SEI on different silicon materials.

SEI Characterization—The overall objective for SEISta is to understand the nature and evolution of the SEI on silicon anodes. The materials standardization and model compounds will enable the researchers to systematically investigate the formation of the solid-electrode interphase using a wide variety of spectroscopy techniques—from different optical, microscopy, and electrochemistry—to determine how the SEI forms based on the nature of the silicon surface, and how it evolves over time. This section of work will continue to grow in scope as we move beyond the sample-characterization phase of the project and toward understanding the

nature and evolution of the SEI. *This part of the project now represents the bulk of the work and, as such, this quarterly report is largely reporting on work leading to this outcome*.

Part 1: Understanding the Thermal Evolution of the SEI

Glyme-Based Electrolytes on a-Silicon Thin-Film Anodes: Surface Chemistry Evaluation

Guang Yang (ORNL), Gabriel Veith (ORNL), Jagjit Nanda (ORNL)

Background

Recent study within SEISta confirms that carbonate-based electrolytes do not effectively passivate the silicon surface like they do for conventional graphitic anodes. Even with the best-performing carbonate electrolyte with addition of a fluorinated carbonate additive, fluoroethylene carbonate (FEC), a finite parasitic or leakage current always exists per our previous corrosion-related reports on a-Si anodes. One possible explanation is that due to the severe volumetric change of Si upon lithiation/delithiation, the sustained reaction between the electrolytes with a freshly exposed silicon surface leads to an unstable SEI with the thickness continuing to increase. One method to solve this issue is to explore solvents and salts other than commonly used carbonate-based electrolytes for Li-ion batteries that could potentially demonstrate better passivating properties on Si. Earlier study by our team investigating SEI formation on amorphous silicon (a-Si) thin film indicates that polymeric ether components such as poly(ethylene oxide) (PEO) are formed during the first couple of galvanostatic cycles (GC),[1] enabling certain viscoelasticity of the SEI to buffer the volumetric change of the Si anodes. We thus hypothesize that the ether functional group-based glyme electrolytes can potentially enrich the PEO oligomer in the SEI, thereby providing better passivation on the Si surface. We have shown that the a-Si thin-film anode with a certain combination of the LiFSI, dimethoxyethane (DME), and fluorinated ether, fluoroether, 1,1,2,2-tetrafluoroethyl-2,2,3,3-tetrafluoropropyl ether (TTE) (denoted as LiFSI-3DME-3TTE) outperforms the best-performing carbonate electrolyte (GenII + 10 wt% FEC). However, the underlying mechanism has not been well explored and understood. It thus motivates us to continue the research on the surface chemistry of the a-Si after GC cycles in Q2. Here, GenII, GenII + 10 wt%, and a fluoroether-free electrolyte, 1.2M LiFSI+DME (denoted as LiFSI-DME), were used as the benchmark. A 50-nm a-Si thin-film anode was used as the model anode, and lithium metal was used as a counter electrode.

Results

The a-Si anodes cycled in different electrolytes were explored by X-ray photoelectron spectroscopy (XPS). The SEI formed on a-Si from both types of electrolyte has complex chemical composition as shown in Figure 1. The first chemical difference between the carbonate SEI (denoted as c-SEI) and the glyme SEI (denoted as g-SEI) worth noting is the peak at 290.8 eV. This peak represents the C 1s core level of the carbonyl carbon in carboxylate compounds (OCOO).[2] The intensity of this peak is noticeably larger in c-SEI from both GenII and GenII-10wt% FEC after 110 GCs compared to g-SEI counterparts. Interestingly, g-SEI on a-Si cycled for 5 times (5 cyc) in LiFSI-3DME-3TTE electrolyte exhibits higher carboxylate abundance than its 110-cyc counterpart. Regardless, the C 1s core level of the ether oxygen centered at 285.7 eV [2] shows a larger intensity than the carbonyl carbon peak for all g-SEIs. This statement is further corroborated by the O 1s core level. The ether oxygen O 1s at 533.0 eV has a comparable intensity with the carbonyl oxygen at 531.9 eV for c-SEI of the GenII(110 cyc) sample. Although the ether oxygen O 1s peak intensity of the c-SEI is only slightly larger than the carbonyl O 1s peak for the GenII-10wt% FEC (110 cyc), the former outweighs the latter for all g-SEI samples. Taken together, it clearly demonstrates that the g-SEI has more ether functional groups than its c-SEI counterparts. Fluorinated species is another group of SEI compounds worth exploring. Shown in the right column in Figure 1, the c-SEI for GenII (110 cyc) has enriched LiP_xF_y components stemming from the decomposition of the $LiPF_6$ salt.[3] The resultant fluorinated species has been found responsible for instability of the c-SEI.[4] Addition of the 10wt% FEC decreased the abundance of the LiP_xF_y component (F 1s core level at 688.7 eV),[5] agreeing with other studies in which the FEC reductive decomposition at the Si surface aids in forming a better and more stable SEI layer,[6] further mitigating the $LiPF_6$ salt reduction. Lacking $LiPF_6$ salt, the intensity of the 688.7-eV F 1s core-level peak for g-SEI drops significantly. Notably, when cycled in LiFSI-3DME-3TTE electrolyte for 5 cycles, there is a shoulder at 688.7 eV for the F1s core level. This may be ascribed to the aliphatic fluoroorganic species derived from the polymerization of the glyme electrolyte

components. According to Ref [7], the peak centered at 686.3 eV is ascribed to Si-F moieties. This indicates that both c-SEI and g-SEI contain abundant fluorinated silicon species. However, for glyme-based electrolytes, the abundance of the fluorinated species was not increased upon adding more TTE. This suggests that the resource of the fluorinated species in the SEI layer on a-Si may stem from the decomposition of the LiFSI salt instead of the TTE additive.

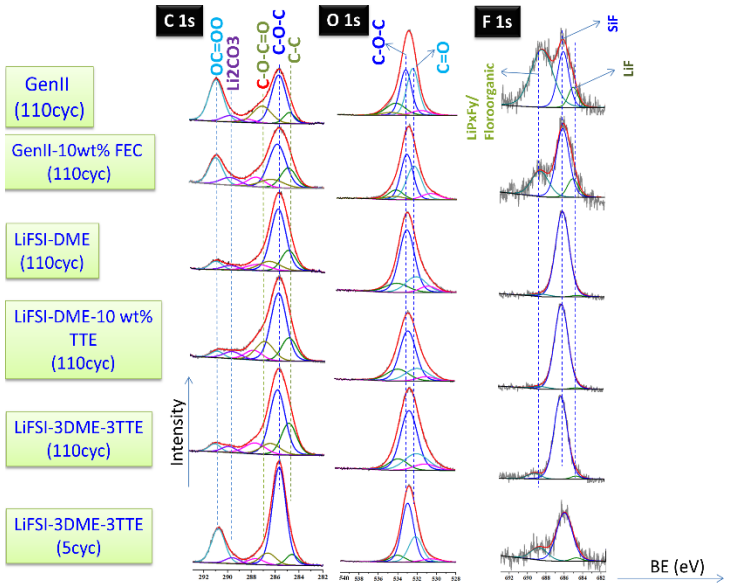

Figure 1. Variation of XPS spectra of the a-Si thin-film anodes cycled in carbonate and glyme electrolytes at three different core levels.

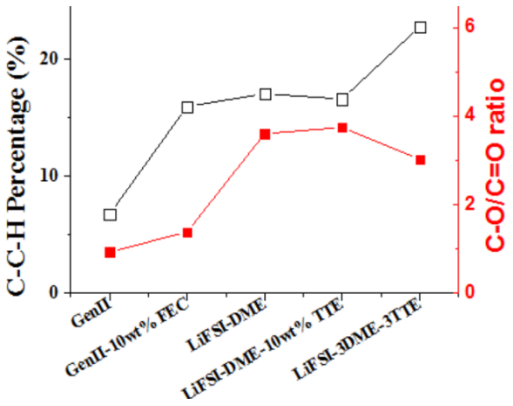

Figure 2. Comparison of the C-C-H moiety atomic percentage and the C-O/C=O ratio based on C 1s core level for 110-cyc a-Si anodes.

Figure 2 shows the relative abundance of a few polymeric moieties in the SEI layer stemming from both carbonate and glyme electrolytes. The aliphatic C-C backbone counts for 7% for GenII electrolyte, but it is more than doubled for GenII-10wt% FEC, LiFSI-DME, and LiFSI-DME-10wt% TTE, suggesting the existence of more than doubled polymeric species. For LiFSI-3DME-3TTE, this value is further increased to 23%, demonstrating that even more polymeric components are derived for g-SEI in this case. Focusing on the C-O/C=O ratio (r), the g-SEI exhibits an r value >12.5%, whereas r is <5% for c-SEI. Taken together, the g-

SEI contains more than twice as much CH_2-CH_2-O repeating unit with respect to inorganic carbonate or carboxylate (C=O) compounds compared to c-SEI counterparts.

Ongoing research includes elucidating and consolidating the surface-chemistry heterogeneity on both of the in-plane and through-plane of the a-Si surface using depth-profile XPS and time-of-flight secondary-ion mass spectrometry. Another future focus is exploring the SEI formation mechanisms following different electrolyte reaction paths in different electrolytes. Proton nuclear magnetic resonance has been measured on various electrolytes after GC cycling at different stages to explore the dissolved SEI species in the electrolytes. Those data are being analyzed and will be reported in due course.

Conclusions

In summary, using XPS, we further evaluate and consolidate the surface chemistry of glyme electrolytes on a-Si thin-film anodes on early and after prolonged cycles. Our results clearly demonstrate that the SEI stemming from the glyme-based electrolytes has enriched polymeric ether compounds than its carbonate counterparts and reduced inorganic carboxylate and carbonate species. This may benefit the elastic behavior of the SEI, capable of accommodating large volume expansion of the Si anodes.

References

1. Nanda, J.; Yang, G.; Hou, T.; Voylov, D. N.; Li, X.; Ruther, R. E.; Naguib, M.; Persson, K.; Veith, G. M.; Sokolov, A. P., Unraveling the Nanoscale Heterogeneity of Solid Electrolyte Interphase Using Tip-Enhanced Raman Spectroscopy. *Joule* **2019**.

2. Yang, J.; Liu, H.; Martens, W. N.; Frost, R. L., Synthesis and characterization of cobalt hydroxide, cobalt oxyhydroxide, and cobalt oxide nanodiscs. *The Journal of Physical Chemistry C* **2010,** *114* (1), 111-119.

3. Aurbach, D.; Markovsky, B.; Shechter, A.; Ein-Eli, Y.; Cohen, H., A comparative study of synthetic graphite and Li electrodes in electrolyte solutions based on ethylene carbonate-dimethyl carbonate mixtures. *Journal of The Electrochemical Society* **1996,** *143* (12), 3809-3820.

4. Yan, J.; Xia, B.-J.; Su, Y.-C.; Zhou, X.-Z.; Zhang, J.; Zhang, X.-G., Phenomenologically modeling the formation and evolution of the solid electrolyte interface on the graphite electrode for lithium-ion batteries. *Electrochimica Acta* **2008,** *53* (24), 7069-7078.

5. Schulz, N.; Hausbrand, R.; Dimesso, L.; Jaegermann, W., XPS-surface analysis of SEI layers on Li-ion cathodes: Part I. Investigation of initial surface chemistry. *Journal of The Electrochemical Society* **2018,** *165* (5), A819-A832.

6. Hou, T.; Yang, G.; Rajput, N. N.; Self, J.; Park, S.-W.; Nanda, J.; Persson, K. A., The influence of FEC on the solvation structure and reduction reaction of $LiPF_6$/EC electrolytes and its implication for solid electrolyte interphase formation. *Nano Energy* **2019,** *64*, 103881.

7. Hantsche, H., High resolution XPS of organic polymers, the scienta ESCA300 database. By G. Beamson and D. Briggs, Wiley, Chichester 1992, 295 pp., hardcover,£ 65.00, ISBN 0-471-93592-1. *Advanced Materials* **1993,** *5* (10), 778-778.

Localized Lithiation of Si with ≥ 5-nm Surface Thermal SiO_2 (NREL)

Paul Stradins, Steve Harvey, Caleb Stetson, Glenn Teeter (NREL)

Background

Control of lithiation rate and SEI formation of the Si electrode is essential to facilitate desired Li-Si alloying reactions, alleviate undesired reduction chemistry, and mitigate the SEI instability. In our previous work, we have galvanostatically cycled the thermally grown oxide films (SiO2, 1.4–3.0 nm) on a Si wafer model system and have shown that the thin oxide films lead to a uniform lithiation of the underlying Si. In contrast, for SiO_2 films thicker than 5 nm, the lithiation occurs locally and is accompanied by pinhole formation, with subsequent lithiation through them. Surprisingly, we also find that the lithiation through pinholes proceeds selectively near the SiO2/Si wafer interface.

In this report, we investigate in more detail the localized lithiation at oxide thicknesses ≥ 5 nm, focusing on microscopic mechanisms and interfacial Li diffusion phenomenon. The anodes were lithiated in half-cells using the O-ring cells presented earlier, which restrict the electrochemically active area to the oxidized front surface of the wafer and eliminate edge effects, and lithiated for 70 h at 10 mV up to a current of 200 nA/cm^2 and a total charge of 2.6 µAh/cm^2.

Results

1. **Optically visible pinhole-lithiated regions are more resistive, likely of silicide phase.**

Pinhole lithiation is accompanied by formation of optically visible disks of about 10–100 microns in diameter. Scanning spreading resistance microscopy (SSRM) resistivity vs. depth profiles were performed inside and outside of these lithiated "discs," see Fig. 1. Both inside and outside the disc (light and dark blue regions, respectively), the resistivity is very high at the surface, suggesting the continued presence of 5-nm oxide. However, this resistivity drops to Si wafer value just after 5 nm from the surface (dark blue curve), but much slower with depth in the lithiated region: inside the ring, there is an increase in electronic resistivity for the Si beneath the SiO_2, consistent with the increase measured from the pristine to the 50-cycle native SiO_x due to amorphization and forming of the silicide phase.

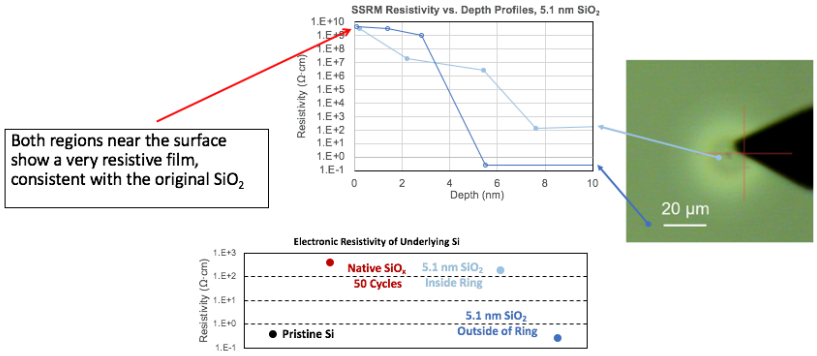

Figure 1. Scanning spreading resistance (SSR) measurements revealing evidence of buried, more conductive bulk phase near pinhole center. Top graph: SSR depth profiles in regions inside (light blue) and outside (dark blue) the lithiated "discs."

Therefore, the optically visible disc (due to the pinhole lithiation) appears to be a different phase (likely silicide and silicate), the oxide appears still somewhat intact even inside the disc, and the silicide phase appears > 10 nm deep. Next, we investigate the chemical composition of these discs using time-of-flight secondary-ion mass spectrometry (TOF-SIMS) and X-ray photoelectron spectroscopy (XPS).

2. **TOF-SIMS shows ~ 10 nm thick new phase within the disc and interfacial Li spreading far outside of the disc.**

TOF-SIMS results are shown in Fig. 2. Inside the optically visible disc (area (c)), Si-bond oxide appears just near the surface (Li bond oxygen appears instead, not shown here), and the Li-rich layer extends about 10 nm deep into the wafer. In contrast, outside the visible Li disc, Si oxide is clearly visible at 5-nm thickness. Surprisingly, there is significant Li accumulation near the Si wafer/ SiO_2 interface even outside the disc. This is further demonstrated by the uniform two-dimensional TOF-SIMS map at z = 5-nm depth (right panel).

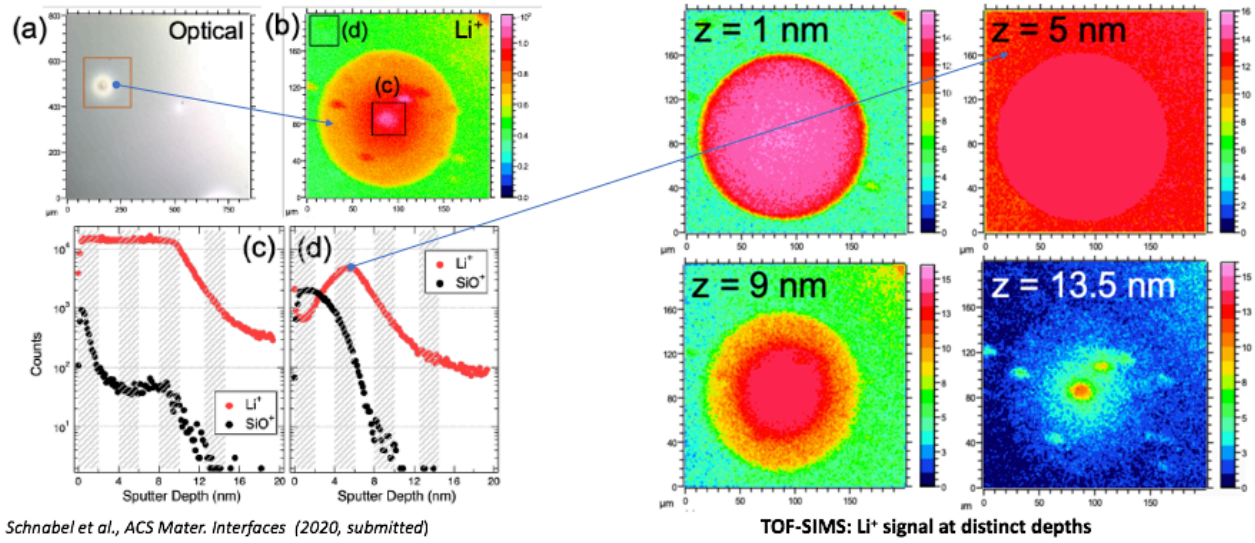

Figure 2. Left: TOF-SIMS map (200μmx200μm) of Li^+ ion showing the Li^+ ion spreading radially ~ 50 μm from a pinhole in SiO_2, with depth profiles near its center ((c), with ~ 10-nm-thick silicide phase, and outside the silicide region (d), Li at the oxide interface). Right: Two-dimensional Li maps at different etch depths, showing interfacial Li diffusion far outside the silicide disc and Li penetration deeper than 13 nm from the pinhole center. Optical image (top left) is 800μx800μm, with TOF-SIMS map subset shown on the image.

Therefore, Li appears to travel far beyond the optically visible silicide/silicate disc. The question is: how did Li get there? There are three possible scenarios: 1) Li entered through the pinhole in SiO_2 and then rapidly diffused along the Si/SiO_2 interface; 2) Li entered through the pinhole and diffused through the Si wafer or SiO_2, accumulating at the interface due to energetical reasons; 3) a fraction of the Li ions entered through the pinhole, but the remaining Li diffused uniformly everywhere else outside the pinhole, via 5-nm-thick SiO_2 layer.

Scenario 2 (diffusion through the Si wafer) is unlikely: diffusion coefficients at room temperature for Li in Si can be estimated to be about 6.5×10^{-14} cm^2/s (see Pratt and Friedman, JAP 37 (1966)), which would give a 70-hour diffusion distance of only about 1 micron. Li diffusion coefficient in SiO_2 can be estimated from the Li+ mobility measurements by Greeuw and Verwey, JAP 56 (1984), using the Einstein relation, giving the diffusion coefficient of about 1.2×10^{-13} cm^2/s, which also results in ~1-micron diffusion distance. Therefore, lateral diffusion with bulk diffusion coefficient values cannot explain the presence of lithium over 50 microns from the pinhole. We turn to the XPS to distinguish scenarios 1 and 3: is Li spreading radially from the pinhole center by interfacial diffusion, but over much longer distances; or is Li uniformly entering the SiO_2 everywhere and just accumulating at the oxide interface?

3. **XPS reveals Li entry via the pinhole, interfacial diffusion, and accumulation at radii far beyond the heavily lithiated disc.**

The XPS mapping (Fig. 3) reveals lithiation-related signatures far beyond the optically visible "lithiated disc" region seen on the upper left panel. That heavily lithiated disc region, as shown previously by TOF-SIMS (Fig. 2), is lithiated to a depth of about 10 nm and here has a radius of about 70 μm. In the same optically visible disc region, the XPS near energies of the Li 1s transition reveals peaks consistent with Li_xSiO_y and Li_xSi, and the valence-band offset vs. Fermi energy in SiO_2 shifts to larger energies of 6.7 eV (not shown here). More importantly, the O1s and Si2p peak shift map also shows disc-like regions with the same centers as the heavily lithiated discs (with radii about 70 μm in Fig. 3), but they extend radially to much longer distances (radii about

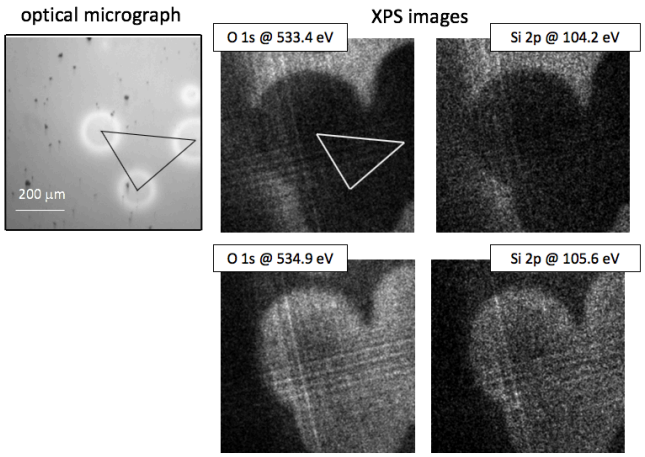

Figure 3. XPS maps of a sample region 800μx800μm in size, showing relative intensities of the O 1s and Si 2p peaks at the energies of the two opposite sides of the respective peaks.

230 μm). These Si 2p and O1s shifts, along with the valence-band offset shift (not shown) in the contrast maps of Fig. 3, are the same as previously observed in the early stages of lithiation by *in-situ operando* lithiation using Li-ion source (Glenn Teeter). Because these peak shift maps show a circular pattern, this "early-stage lithiation" appears consistent with Li entry via the pinhole and rapid lateral diffusion along the SiO_2/Si wafer interface, rather than uniform Li penetration from the surface of the SiO_2. This scenario (1) then implies interfacial Li diffusion coefficients ~ 10^4 times exceeding those in the bulk Si and bulk SiO_2. Alternatively, that process might be interfacial-reaction limited. Very large current densities are required to reconcile the pinhole entry with the electrochemistry results reported earlier. Further studies are also needed to confirm this effect on large-scale TOF-SIMS maps of the size similar to the XPS mapped regions in Fig. 3.
Conclusions (relating to Q4 and Q3 milestones) are as follows:

1. Lithium enters oxidized Si (thermal oxide $\geqslant$ 5 nm) via sporadic pinholes located millimeters apart.

2. TOF-SIMS maps reveal large regions of Li interfacial accumulation and smaller circular lithiated islands ~ 10 nm deep and ~ 70 microns in radius. XPS maps reveal regions with no Li, Li at the interface, and $LiSi_x$.

3. Li spreads radially along the Si/SiO_2 interface ~ 100 microns in 70 h, with effective diffusion coefficients 10^3–10^4 times exceeding the bulk diffusion of Li in Si and SiO_2.

4. As Li spreads along the interface, eventually a ~10-nm-thick $LiSi_x$ compound disk of a smaller diameter (tens of microns) is formed around the pinhole.

5. Fast Li spreading along the interface might be a combination of fast interfacial diffusion and reaction. Time series might reveal the mechanisms. Experiments on n-type wafers might reveal the role of electric field. This phenomenon might be useful for future battery design.

Part 2: Understanding Zintl Phase Stabilization of the SEI

Mechanistic Understanding of Zintl Phase in the SEI Using Model Systems

Zhifei Li, Yeyoung Ha, Mike Carroll, Sarah Frisco, Jessica Dudoff, Glenn Teeter, Caleb Stetson, Andrew Norman, Chun-Sheng Jiang, Andriy Zakutayev, Sang-Don Han, Nathan Neale (NREL), Xiang Li, Baris Key, Jack Vaughey (ANL)

Background

Recently, Han and Key et al. reported an enhanced electrochemical performance of Si powder-based electrodes (with 10 wt % hard carbon additive (C45) and 10 wt % lithium polyacrylate binder (LiPAA)) in the presence of 0.1 M $Mg(TFSI)_2$ in GenF electrolyte (1.2 M $LiPF_6$ in EC:EMC (3:7 wt%) + 10 wt% FEC).[1] The main idea of this study is the co-insertion of Mg and Li cations into the Si electrode during the lithiation process, forming less-reactive metal-substituted lithium silicide species in an *in-situ* manner and reducing the reactivity of charged Si anodes, which result in improved electrochemical performance. Post-electrochemistry characterizations demonstrate that adding Mg secondary salt leads to the co-insertion of Mg cation along with Li into Si during the lithiation process to form relatively stable Li-Mg-Si ternaries. Further *ex-situ* (and *in-situ*) characterization, however, are still required to address these questions for a better understanding of Li-Mg-Si Zintl phase within a silicon-electrolyte interphase (SEI):

- What is the formation mechanism of Li−M−Si Zintl phase (e.g., surface *vs* bulk reactions and ion diffusion *vs* ion exchange)?
- What is the effect of Li−M−Si Zintl phase on SEI?
- Where does MgO come from (e.g., trace amount of water in an electrolyte *vs* SiO_2), and what is the role of MgO in SEI (e.g., insulating the surface *vs* preventing further reactions)?

Due to the complexity of the SEI and decomposition products—as well as active materials, binder, and conductive carbon in composite electrodes and the limited characterization capabilities with composite electrodes—there is a need for study of model electrodes such as an amorphous silicon thin film, a silicon wafer, and a silicon nanoparticle instead of Si composite electrodes. In addition, the cation and anion of the secondary salt, the starting Si material, and the electrolyte solvent choices can have effects on the electrochemical performance of the silicon full cell. So, more systematic and fundamental studies are critically required.

Results

Analysis of electrochemically lithiated amorphous Mg coated Si thin film as a model electrode

Last quarter, we studied the formation mechanism of Li-Mg-Si Zintl phase using Mg-coated Si thin film as a model electrode. From our preliminary results, we found that the coated Mg can diffuse into the bulk Si layer and form the Mg_2Si layer, and this Mg coating significantly improved the cycling performance of Si anode by potential formation of Li-Mg-Si Zintl phase. This quarter, we performed further characterization of the electrochemically lithiated Mg-coated Si thin film and synthesized Mg_2Si as the reference material to obtain further information about the formation of ternary Li-Mg-Si Zintl phase.

In the last report, we demonstrated the diffusion of Mg into the bulk Si layer via scanning spreading resistance microscopy (SSRM) and focused ion beam (FIB)-transmission electron microscopy (TEM) energy-dispersive X-ray spectroscopy (EDS) mapping. To further analyze the property of the Mg-coated Si thin-film electrode (Si/Mg), we prepared Mg_2Si as a reference material to build a chemical reference library for binary Mg-Si

Zintl phase. The reference Mg_2Si was synthesized by depositing 120 nm of Mg on top of a 60-nm Si thin film based on a Cu foil as the substrate, then heating up the films at 330°C under Ar atmosphere. At this ratio, the Si should be in excess upon the formation of Mg_2Si, which ensures that all the Mg is converted into Mg_2Si. The formation of Mg_2Si was proved by X-ray diffraction (XRD, Fig. 1a), where the XRD pattern of the obtained Mg_2Si film agrees with the standard XRD pattern of Mg_2Si. In addition, Raman spectra were collected for the synthesized Mg_2Si, Si/Mg, and Si film electrodes (Fig. 1b). The Mg_2Si film exhibits peaks at 120, 256, and 344 cm^{-1}, respectively. The peak at 120 cm^{-1} has not been identified, which may be attributed to the Mg phase; the peaks at 256 and 344 cm^{-1} are due to the F_{2g} and F_{1u} phonon band of Mg_2Si, respectively. The pure Si film shows only two broad peaks at around 150 and 469 cm^{-1}. In the case of the Si/Mg film, it shows two small peaks at 120 and 254 cm^{-1}, and one broad peak around 344 cm^{-1}, indicating that a minor amount of Mg_2Si was formed in the Si/Mg film upon the deposition of the Mg layer on the Si thin film.

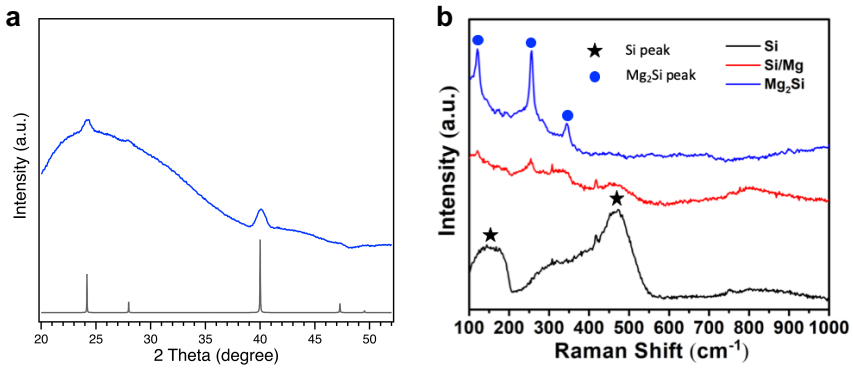

Figure 1. a) XRD pattern of Mg_2Si deposited on glass substrate and b) Raman spectra of pristine Si thin film, Mg-coated Si thin film (Si/Mg), and synthesized Mg_2Si.

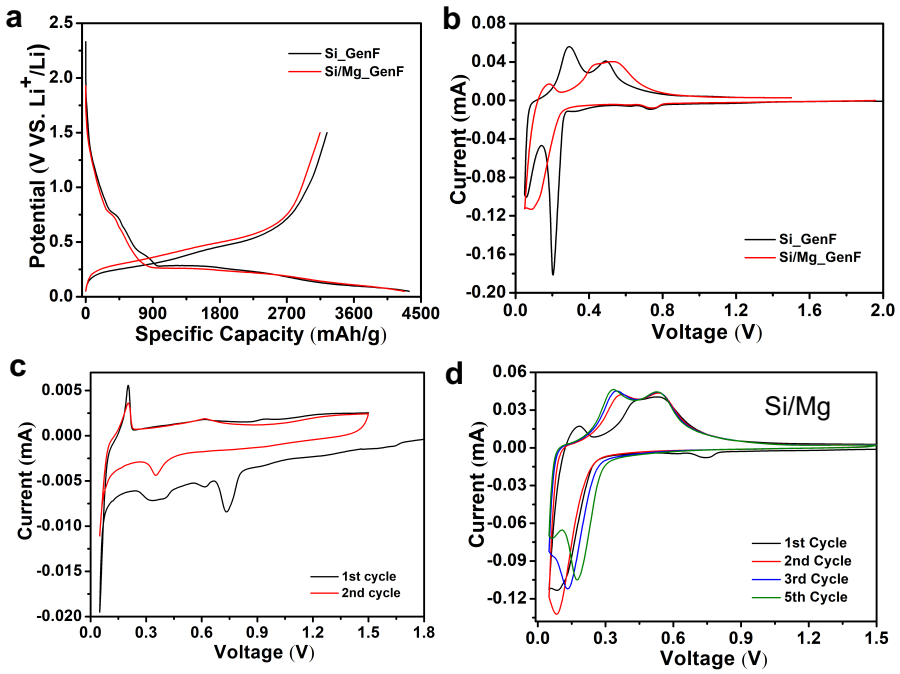

Figure 2. Electrochemical characterization of pure Si and Si/Mg thin-film electrodes with GenF electrolyte. a) The first galvanostatic charge-discharge profiles under current density of 0.1 C in the potential range of 0.05–1.5 V, b) The first CV

cycle under scan rate of 0.1 mV/s in the potential range of 0.05–1.5 V, c) The first two CV cycles of 20-nm Mg deposited on copper foil in GenF electrolyte under scan rate of 0.1 mV/s in the potential range of 0.05–1.5 V, and d) The five CV cycles of Si/Mg in GenF electrolyte under scan rate of 0.1 mV/s in the potential range of 0.05–1.5 V.

The electrochemical performance of Si/Mg and pure Si thin-film electrodes were evaluated in Li half-cells with the GenF electrolyte (Fig. 2a). The first reversible capacities of Si and Si/Mg thin-film anodes are 3,240 and 3,145 mAh/g, respectively. The relatively lower capacity of Si/Mg compared with Si may be due to the reduced Li^+ ion diffusivity and the increased polarization within/near the Mg layer. During the first charge-discharge cycles, both the Si and Si/Mg anodes show a small plateau around 0.75 V (*vs* Li/Li^+, hereafter), which should be due to SEI formation, and this agrees with the small irreversible peak around 0.75 V during the first cathodic scan in the cyclic voltammetry (CV, Fig. 2b). The additional small plateau of pure Si thin-film electrode in the potential range of 0.26–0.50 V during the first discharge should be due to the lithiation of some minor native SiO_2 on the surface of the electrode. In the first CV cycle, the Si thin-film electrode exhibits two cathodic peaks at around 0.2 and 0.05 V, and two anodic peaks at around 0.29 and 0.49 V, which are due to the Li-Si alloying and dealloying process, respectively. In contrast, the Si/Mg thin-film electrode shows only one broad cathodic peak in the potential range of 0.25–0.05 V and one broad anodic peak in the potential range of 0.4–0.6 V. These broad redox peaks of Si/Mg during the first CV cycle demonstrate the large polarization of Si/Mg induced by the Mg coating. The Si/Mg also displays an extra anodic peak at around 0.18 V, which should be due to Li-Mg dealloying process. We performed additional CV tests with 20-nm pure Mg thin film deposited on copper foil to confirm the Li-Mg (de)alloying process. The pure Mg electrode also displays an anodic peak at around 0.2 V with a sharp cathodic peak around 0.05 V (Fig. 2c), confirming the Li-Mg (de)alloying process in this potential range. Note that this Li-Mg dealloying peak of Si/Mg disappears in the following CV cycles (Fig. 2d), indicating that there is no pure Mg layer after the first CV cycle. In addition, the one broad cathodic peak of Si/Mg in the first CV cycle splits into two peaks at the fifth cycle, and the broad anodic peak splits into two anodic peaks at the second cycle and further shifts to a lower potential at the fifth cycle. All these observations indicate that the polarization of Si/Mg decreases upon prolonged cycling. The disappearance of the Li-Mg dealloying peak, the decreased polarization, together with the initial diffusion of Mg into the bulk Si layer suggest that the lithiation/delithiation process accelerates the Mg diffusion process and increases the Li^+ ion diffusivity in the Si/Mg electrode.

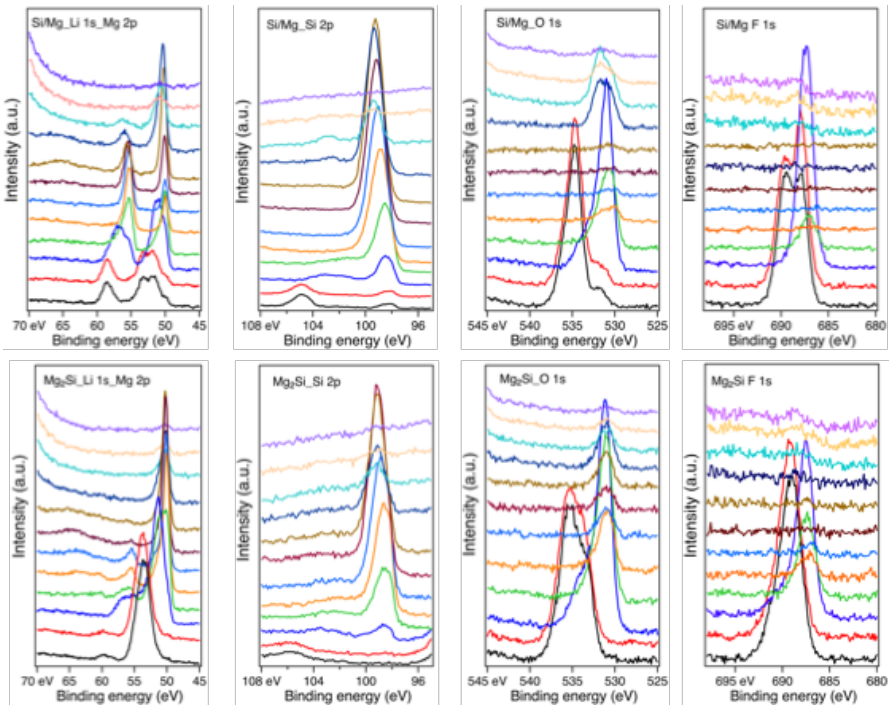

Figure 3. The XPS depth profiles of Li 1s, Mg 2p, O 1s, and F 1s for both Si/Mg and the reference Mg_2Si electrodes.

We performed XPS depth profiling of both Si/Mg and reference Mg_2Si thin-film electrodes to understand the reasons for electrochemical performance improvement and the formation mechanism of potential ternary Li-Mg-Si Zintl phase. The XPS depth profile of Li 1s, Mg 2p, Si 2p, O 1s, and F 1s for both Si/Mg and Mg_2Si are shown in Fig. 3. Most of the spectra shift to lower binding energies after the first two sputtering cycles, except the Si 2p peaks, which is attributed to the charging effect of the surface SEI. The reason that the Si 2p does not shift to lower binding energies may be due to the small amount of the Si detected on the surface and the existence of native SiO_2. In addition, the Si 2p peaks seem to shift to higher binding energies in the following cycles, indicating its change in oxidation state. The Mg 2p peak remains consistent in the Si/Mg through the bulk, which further proves that Mg diffuses into the bulk Si layer and the lithiation may accelerate this process. There is almost no oxygen in the bulk layer of Si/Mg electrode, whereas there is slightly more oxygen in the bulk layer of the reference Mg_2Si electrode, which may be introduced into it during the heating process. The F 1s spectra disappear after several sputtering cycles for both electrodes because F exists only in the SEI as SEI components.

The XPS Li 1s, Mg 2p, and Si 2p spectra from the bulk layer after 14 sputtering cycles were further analyzed to study the possible formation of Zintl phase (Fig. 4). In both Si/Mg and Mg_2Si thin-film electrodes, most of the Li 1s is associated with ternary Zintl phase with some minor contribution from Li_2O. Note that after the same sputtering cycles, the Si/Mg contains more Li than the Mg_2Si electrode, which should be due to the slow lithiation kinetics of Mg_2Si. For Mg 2p, both of the electrodes display a sharp Mg 2p peak, where the main component is associated with Zintl phase with minor contribution from MgO. The Si 2p peaks for both electrodes originate from the bottom Si layer and Si from Zintl phase. The existence of Si^0 peak suggests that the electrode have not been fully lithiated after the first lithiation. The O 1s peak of Mg_2Si is much higher than that of Si/Mg, so there is more oxygen at this depth for Mg_2Si, which is related to Li_2O, MgO, and SiO_x. Overall, both the Mg 2p and Si 2p results suggest the formation of Li-Mg-Si ternary Zintl phase of the Si/Mg anode upon lithiation, even though its composition is different from that of the Mg_2Si anode. Note that it is possible that the Si/Mg may have just formed Li_xSi and Mg_2Si rather than ternary Zintl phase after the first

lithiation. However, even if that occurred, the Mg_2Si could still be converted into ternary Zintl phase in the following lithiation cycles. Therefore, the XPS depth profiling with the reference Mg_2Si electrode demonstrates that the introduction of Mg coating on the surface of the Si thin anode could lead to the formation of Li-Mg-Si ternary Zintl phase upon lithiation, which alters the surface SEI and improves the cycling stability of the Si anode.

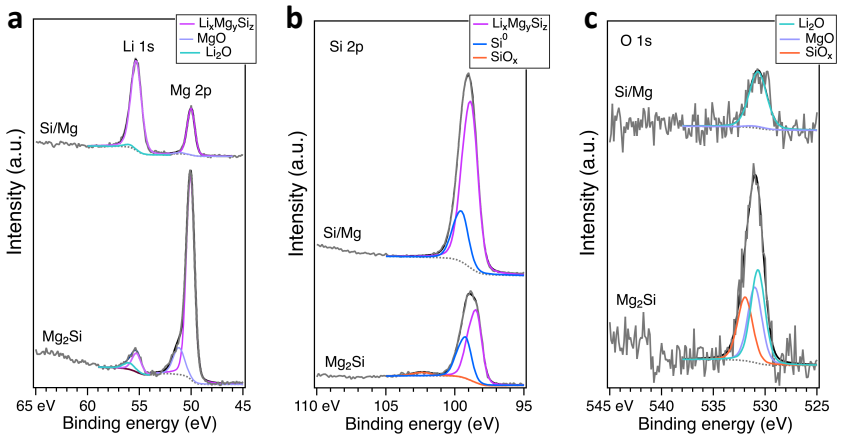

Figure 4. High-resolution XPS spectra of the Si and Si/Mg electrode after the first lithiation in GenF electrolyte obtained from depth profiling after 14 sputtering cycles with Ar ion: a) Li 1s and Mg 2p, b) Si 2p, and c) O 1s.

The previous SSRM, cross-section EDS mapping associated with TEM, together with the Raman results can suggest that the coated Mg diffuses into the bulk Si layer. The XPS depth profiling after lithiation proves the relatively uniform distribution of Mg in the bulk layer and the possible formation of ternary Zintl phase. The above results suggest that the Mg diffusivity within the amorphous Si thin film plays a critical role in the formation of ternary Zintl phase, where the lithiation of the coated electrode would further accelerate the diffusion of Mg and the formation of Zintl phase.

XPS analysis of potential Zintl phase formed on a Si wafer and synthesized Li_2MgSi model compound

Last quarter, we developed Si wafer electrodes as a model system to study the Li-Mg-Si Zintl phase formation mechanism. The electrodes were lithiated in GenF and GenFM (GenF + 0.1 M $Mg(TFSI)_2$), and the lithiated electrodes were analyzed with XPS. The XPS depth-profile analyses showed that a thinner SEI layer formed in GenFM and the presence of MgO in the SEI layer. This quarter, H-terminated Si wafers were employed to determine the effect of surface SiO_x on Zintl phase formation and to examine the source of MgO. In addition, a Li_2MgSi model compound prepared by ANL was analyzed using XPS to build a reference library for Zintl phase.

To obtain a H-terminated surface, the native oxide layer on Si wafer electrodes (6 mm × 6 mm × 675 µm, 0.001–0.005 Ω cm, p-type (B)) was removed via HF etching. Then, the H-terminated Si wafer electrodes were immediately transferred to the glovebox antechamber, dried under dynamic vacuum for 30 min, and assembled into Si/Li coin cells using GenF and GenFM. After 2 h of rest, the cells were galvanostatically discharged at 100 µA/cm^2 for 2 h, followed by potentiostatic hold at 10 mV for 40 h. The electrochemical response of Si/Li half-cells in GenF and GenFM are shown in Fig. 5. After the potentiostatic hold, the cells were disassembled in the glovebox, and the electrodes were rinsed in 1 mL of DMC for 60 s to remove residual electrolyte. The native oxide and H-terminated Si wafer electrodes showed a very similar current evolution profile during the potentiostatic hold (i.e., continuous growth of current in GenF *vs* quick decay in GenFM), but the texture of the lithiated electrodes appeared to be different (i.e., shiny surface on the native oxide Si *vs* dark, matte surface on

the H-terminated Si). The electrochemically treated samples were transferred to the XPS chamber without exposure to air.

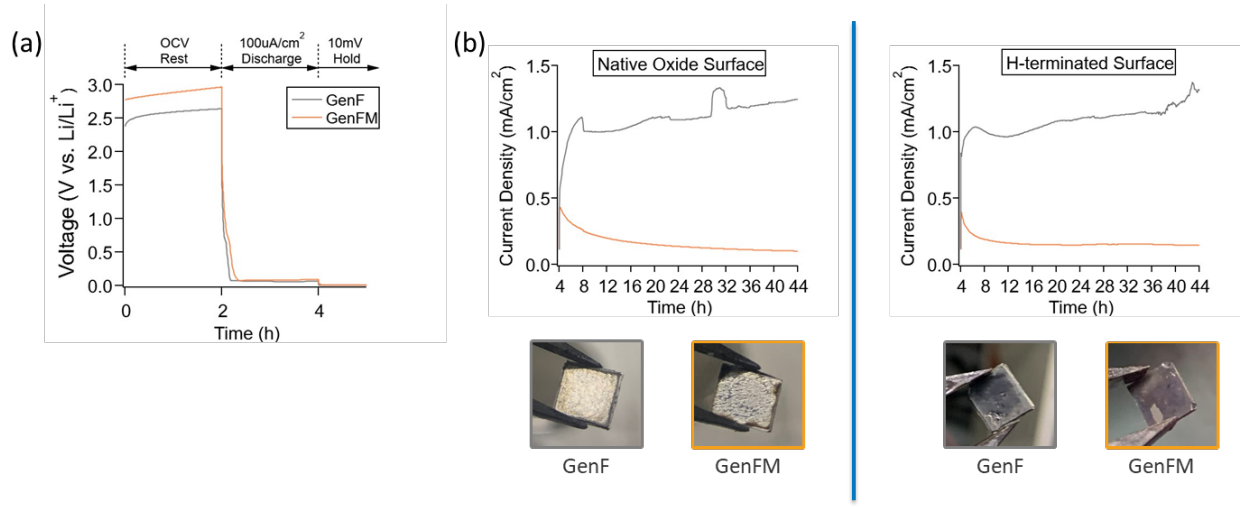

Figure 5. (a) Electrochemical lithiation protocol of Si wafer electrodes in GenF (gray) and GenFM (orange). (b) Current evolution during the 10-mV potentiostatic hold (top) and photographs of lithiated Si wafer electrodes (bottom). Native oxide Si wafer results are shown for comparison.

XPS depth profile analysis was performed on the lithiated H-terminated Si wafer samples. The SEI layer was removed via Ar^+ sputtering at ~4 nm/min rate, and spectra were collected every minute. The results are shown in Fig. 6. First, in the GenF depth profile data, one noticeable difference between the native oxide Si (FY20 Q1 report, Fig. 4) and the H-terminated Si is that the Si2p core-level peaks appear after a shorter length of sputtering in H-terminated Si (1 min *vs* 5 min for native oxide Si). In addition, the ~3-eV charging observed initially in the SEI species also follows the same trend. For example, carbon-containing species (e.g., C-C/C-H, C-O, and O=C-O) disappear after 1 min of sputtering in the H-terminated Si, whereas they disappear after 5 min of sputtering in the native oxide Si. Such behavior may indicate a thinner and/or easily sputtered SEI layer formation in the absence of surface SiO_x. Although the GenFM depth profile data exhibited a much thinner SEI layer compared to that formed in GenF on the native oxide Si electrodes (FY20 Q1 report, Fig. 5), the rate at which the SiEI species disappear seems to be similar in GenF and GenFM on the H-terminated Si electrodes. The SEI species (carbon-containing species and LiF) are detected up to a longer sputter depth on the H-terminated Si electrodes lithiated in GenFM compared to that on the native oxide Si lithiated in GenFM. Hence, it may be possible that the SEI layer formed on the H-terminated Si electrodes has a different morphology and composition compared with the native oxide Si electrodes.

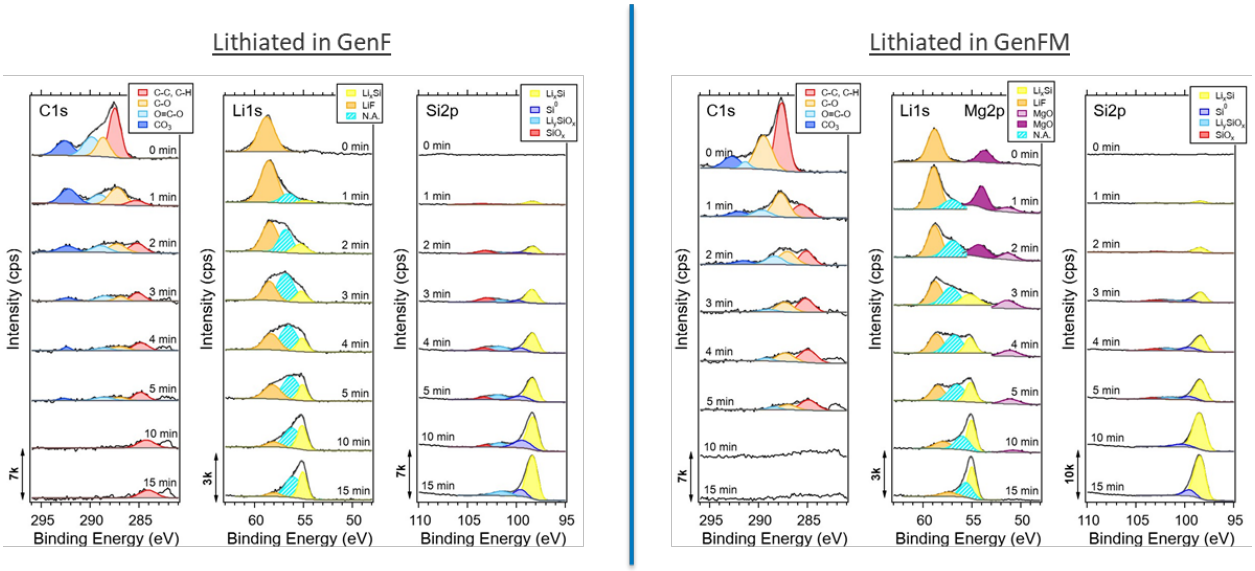

Figure 6. XPS depth-profile analysis of H-terminated Si wafer electrodes lithiated in GenF (left) and GenFM (right). Spectra at selected sputter depth are shown (sputter rate = ~4 nm/min). C 1s, Li 1s, Mg 2p, and Si 2p core levels are presented with raw spectra (black line) and the fit (gray line). Peak assignments are preliminary.

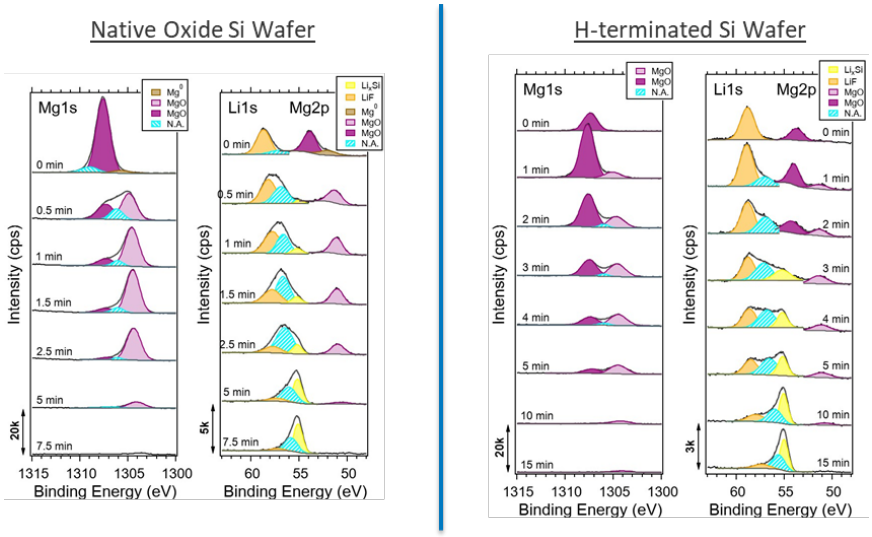

Figure 7. Comparison of Mg 1s and Mg 2p core levels in native oxide (left) and H-terminated (right) Si wafers lithiated in GenFM. Spectra at selected sputter depth are shown (sputter rate = ~4 nm/min) with raw spectra (black line) and the fit (gray line). Peak assignments are preliminary.

Comparison of the XPS depth-profile spectra of Mg core levels (Mg 1s and Mg 2p) in the native oxide and H-terminated Si electrodes are shown in Fig. 7. Interestingly, two peaks with ~3-eV separation (~1,038 and ~1,035 eV in Mg 1s, and ~54 and ~51 eV in Mg 2p core levels) are detected in both electrodes, albeit different intensity ratios. One of the possible explanations for these two peaks is that there may be charged and not charged MgO species giving rise to two different peaks, depending on the neighboring species and their conductivity. For example, the ~3-eV charging observed in the SEI species went away upon sputtering for certain species (e.g., C-C/C-H, C-O, and O=C-O), whereas some other species (e.g., CO_3 and LiF) remain throughout the sputtering. Thus, it is possible that the MgO species bound to the former species give rise to the

lower binding-energy peak, whereas those bound to the latter species remain charged and continue to appear at a higher binding energy. Also, note that the lower binding-energy peaks show the highest intensity as the Si species peaks emerge, suggesting the lower binding-energy MgO species may be directly bound to the Si electrode surface. Another possible explanation for the existence of the two peaks is that each peak could be representing two different species, MgO and MgF_2. The two species have very similar binding energies, so it is challenging to distinguish those from Mg core levels. Nonetheless, depending on the nature of the material, they may show different charging behavior upon sputtering, where one species is being charged whereas the other one is not. Due to strong overlapping peaks in O 1s and F 1s core levels, however, additional peaks associated with MgO and MgF_2 cannot be clearly located.

To build a reference library of XPS binding energies for Li-Mg-Si Zintl phase, a Li_2MgSi model compound was analyzed. The material was cleaved inside a glovebox to expose a fresh surface and was immediately transferred to the XPS chamber without exposure to air. However, within ~10 min of the sample transfer time, the surface was already oxidized and contaminated as shown in Fig. 8. After ~45 min of Ar^+ sputtering, the impurities (e.g., Li_2O, Li_2O_2, MgO, C-O) were largely removed. Additionally, the intensities of three peaks from Si 2p (~98.7 eV), Li 1s (~55.2 eV), and Mg 2p (~49.8 eV) core levels increased greatly, which may potentially be coming from the Zintl phase material. However, the calculated ratio of Li:Mg:Si from these peaks was 9:1:8, which is different from the expected stoichiometry (2:1:1). In an attempt to restore the atomic ratio on the surface, the sample was annealed at a higher temperature by heating it inside the XPS chamber under vacuum. As the sample was heated (Fig. 8), the concentration of Mg on the surface increased. However, the oxygen signal also increased simultaneously, and a peak at a higher binding energy evolved in the Mg 1s core level, indicating the formation of MgO on the surface. This trend was observed during iterations of sputter cleaning and heating. Thus, heating the material created mobile Mg, which moved closer to the surface but only in the form of MgO.

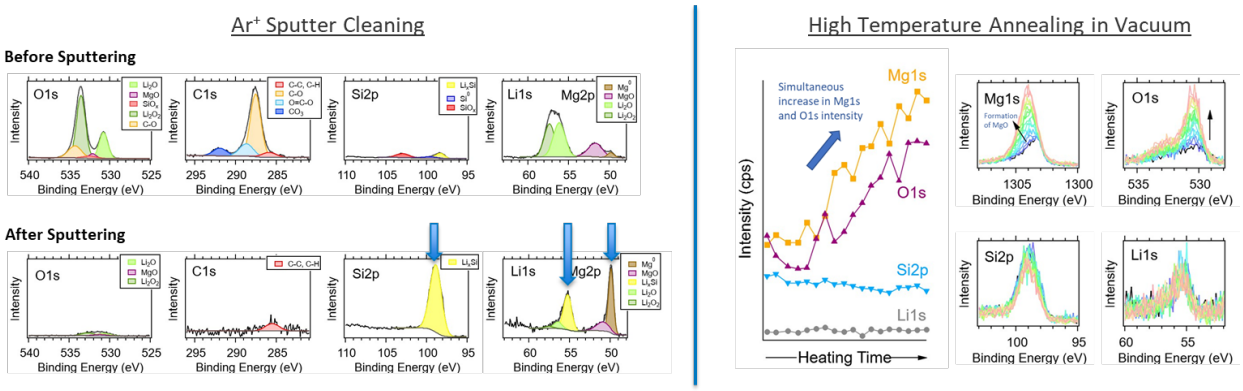

Figure 8. XPS analysis of Li_2MgSi model compound. The surface was cleaned via ~45 min of Ar^+ sputtering (left) and annealed by heating the sample in vacuum (right). Blue arrows in Si 2p, Li 1s, and Mg 2p core-level spectra obtained after the sputter cleaning indicate potential Zintl-phase peaks. Peak assignments are preliminary.

Probing the electrochemical capacity retention properties of potential Zintl phase formed on size- and surface-varied silicon nanoparticle-based composite electrodes.

To date, the only composite anode system with which the Zintl phase chemistry was demonstrated was on electrodes fabricated by the CAMP facility (at ANL) using commercially available silicon nanoparticles (Si NPs, Paraclete Energy). Moreover, the same electrolyte applied to a different batch of Paraclete silicon electrodes (fabricated in the same way) showed that the $Mg(TFSI)_2$ had a negative effect on the cycling. This

observation raises questions about the parameters that effect the Zintl phase chemistry at Si NPs. The Paraclete Si NP is 150 nm in diameter on average and has a surface SiO_2 layer that is 2–3 nm thick. In addition, the carbon content of this silicon appears to vary from batch to batch. Therefore, to better understand the active materials chemical conditions needed to realize the benefit of Zintl phase formation on silicon, we performed a parametric analysis of the role on Si NP size, surface oxide layer, and cycle rate on the capacity retention of composite anodes. This helps to address the Quarter 2 milestone "Have determined Zintl phase formation mechanism and its effect on SEI with model systems including Si NPs, Si wafer, a-Si thin film using XPS, AFM/SSRM, STEM-EDS, and FTIR/Raman."

Using silicon synthesized from RF non-thermal plasma methods at NREL, composite electrodes were fabricated from silicon with SiH_x-terminated surfaces for a series of Si NP sizes (ranging in diameter from 3.5–33.5 nm). Figure 9a plots the normalized electrochemical cycling properties at a cycle rate of C/5 of these silicon composite electrodes with Gen2, GenF (Gen2 + 10% FEC), and GenFM (GenF + 0.1M $Mg(TFSi)_2$). From these data, the large particles, in general, display a much lower capacity retention than the smaller Si NPs. This trend is independent of electrolyte composition. However, the electrolyte also impacts the capacity fade rate, where GenF-based electrodes have the best capacity retention, followed by GenFM, and finally, Gen2. The reduced capacity retention with GenFM electrolyte compared to GenF contradicts the expected results based on prior studies.[1] To quantify the capacity fade rate, these data were fit to a single-exponential function and the "lifetime" (defined here as the formal exponential lifetime [initial capacity × 1/e] ~ 30% retention) of those exponential fits is shown in Fig. 9b for a cycle rate of C/5. The data in Fig. 9b show the same trends as the raw data: smaller silicon NPs consistently outperform larger ones (3.5 *vs* 30 nm) for capacity retention, and the electrolyte impacts capacity retention for all Si NP sizes where GenF > GenFM > Gen2 when cycled at an equal rate of C/5. The capacity retention lifetime spans several orders of magnitude, from 10s of cycles (large silicon in Gen2 electrolyte) to 1000s of cycles (small silicon in GenF electrolyte). To probe the role that surface oxide layers have on these Si NPs, we intentionally oxidized a fraction of our otherwise SiH_x-terminated Si NPs and then assembled those oxidized particles into electrodes, and eventually coin cells, in the same way as the SiH_x-terminated silicon. From the scatter plot in Fig. 9, the presence of an oxide layer appears to have little effect on capacity retention when compared to the effect of size or electrolyte.

Forming Zintl phase compounds at the surface of silicon during electrochemical cycling against lithium could, in principle, reduce the negative mechanical effects by providing a scaffold to the silicon through kinetically trapped (metastable) Si/Mg phases. This could manifest an improvement in the capacity retention at fast cycle rates. To test this hypothesis, we carried out the same cycling procedures as described above but accelerated the cycling rate to 1C. The lifetime data from that experiment are shown in Fig. 9c. From Fig. 9c, the electrodes with either Gen2 or GenF display nearly identical capacity retention characteristics as those measured under a C/5 rate. However, with $Mg(TFSI)_2$ present, the trend changes: the GenFM-based coin cell significantly improves in capacity retention for all silicon sizes. Indeed, the GenFM capacity retention at 1C for intermediate Si NP sizes ($6 < d < 15$ nm) is better than that of the GenF at a C/5 cycle rate. We note, however, that when a surface oxide is grown on the surface of these silicon particles, the effect of $Mg(TFSI)_2$ is lost. This is indicated by the drastically reduced capacity retention lifetimes of the SiO_2/Si. Nevertheless, these data hint at the tantalizing possibility that Zintl phase formation can induce kinetic trapping (metastable phases) in the silicon during lithiation/delithiation, which reduces mechanical degradation modes in silicon at fast rates. This may also improve the lithium diffusion kinetics in GenFM-based electrolytes.

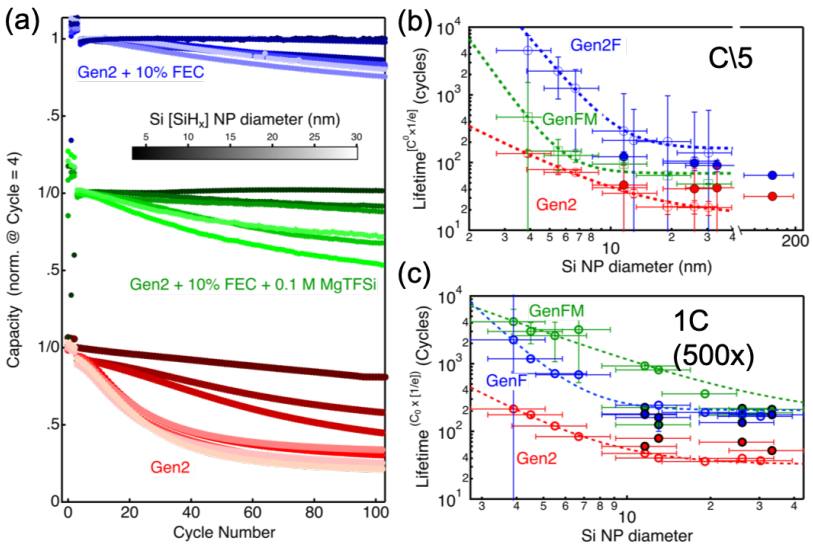

Figure 9. (a) Normalized cycle capacity fade plots for a size series of Si NP-based composite anodes with Gen2 (red), GenF (blue), and GenFM (green) electrolytes in a LIB half-cell configuration against lithium metal. These electrodes were electrochemically cycled for 3 cycles at C/20 (forming) and 100 cycles at C/5 between 0.01–1.5 V. The hue of the color indicates the average NP size (scale bar). (b) Scatter plot of the fitted exponential lifetimes to the data in Fig. 9a. The open shapes correspond to Si NPs with SiH_x surface termination, and the closed shapes are those with a SiO_2 surface layer. The vertical error bars are the error from the fitting procedure, and the horizontal error bars are $\pm$ 1σ from the mean diameter of the silicon particle. (c) Scatter plot of the fitted exponential lifetimes for the same electrodes as Fig. 9a, but the electrochemical cycle rate has increased to 1C and the electrodes were cycled 500 times.

Conclusions

Amorphous Mg-coated Si thin film was prepared by magnetron sputtering as the model electrode to study the mechanism of Zintl phase formation. It was revealed that the coated Mg was able to diffuse into the bulk Si layer upon deposition at room temperature, and this process could be accelerated by electrochemical lithiation. XPS depth profiling proves the possible formation of ternary Li-Mg-Si Zintl phase. The formed Zintl phase alters the SEI properties, suppresses the electrolyte decomposition, and significantly improves the capacity retention of the Si thin-film anode. This study provides insights about the possible mechanism of Zintl phase formation, and a more detailed formation mechanism study is still ongoing with different controlled samples.

H-terminated Si wafer electrodes were examined via XPS depth profiling, and the results were compared with the spectra obtained from the native oxide Si wafer electrodes. In both H-terminated and native oxide Si wafer electrodes lithiated in GenFM, MgO was detected in the SEI layer, but there was no clear evidence of Zintl phase formation. Considering the lesson from synthesized Li_2MgSi as a reference Zintl phase material that has an extremely high reactivity—where Li and Mg oxides can be formed on the surface within 10 min after the fresh surface is exposed in an inert atmosphere—it is possible that the Zintl phase exists in/on the electrode, but that observing the species with surface-sensitive *ex-situ* measurements such as XPS is quite challenging. Nonetheless, evaluating the surface composition and determining the binding energies associated with different Mg-containing species is critical to understanding the Zintl phase formation mechanism. Thus, we plan to continue our efforts to understand this system by using Auger electron spectroscopy on composite electrodes to look at a single Si NP in the composite electrode, in combination with depth profiling. In addition, scanning transmission electron microscopes–energy-dispersive X-ray spectroscopy measurement will be performed to look at the cross section of nanoparticles and the atomic distribution.

Three major conclusions from our studies of size- and surface-varied Si NP-based composite electrodes are as follows:

- Small Si NPs increase the capacity retention in otherwise identical composite anodes.
- The electrolyte plays a large role in capacity retention, where, at C/5, the Zintl phase chemistry appears to hinder the capacity retention compared to GenF.
- At faster cycle rates (1C), the Zintl phase chemistry improves the electrode capacity retention, which suggests that the role of $Mg(TFSI)_2$ may be related to kinetic parameters such as forming metastable phases.

References

1. B. Han, C. Liao, F. Dogan, S. E. Trask, S. H. Lapidus, J. T. Vaughey, B. Key, Using Mixed Salt Electrolytes to Stabilize Silicon Anodes for Lithium-Ion Batteries via In Situ Formation of Li−M−Si Ternaries (M = Mg, Zn, Al, Ca). *ACS Appl. Mater. Interfaces* 11, 29780 (2019).

Part 3: Understanding Silicon Alloys Effect on the SEI

Silicon-Tin Alloys

Terri Lin, Elisabetta Arca, Insun Yoon, Robert Kostecki (LBNL)

Background

Si has garnered tremendous interest as a replacement for graphite in lithium-ion battery (LIB) technology due to its potential to enable lighter-weight and lower-cost battery packs for large-scale applications such as electric vehicles and grid-scale storage. Si is primarily attractive due to its large capacity (4,200 mAh/g, which is 10 times higher than graphite) and low market price. However, commercial devices with high Si content are limited by the following pitfalls: 1) Si undergoes significant structural reconstruction and volume change during charge/discharge. This results in substantial strain within the material and leads to the propagation of cracks and material loss, resulting in a rapid capacity fade. 2) The Si/electrolyte interface is unstable during electrochemical cycling. The solid-electrolyte interphase (SEI), which consists of various electrolyte decomposition products, does not fully passivate the Si surface. Consequently, electrolyte and Li+ are continually consumed, and this results in an irreversible capacity loss. To date, only a limited fraction of Si (~15 wt.%) has been incorporated in graphite anodes to increase the energy density without sacrificing the lifetime. Significant efforts must be made to achieve further improvements.

The use of nanostructured Si-electrodes and intermetallics (metal compounds with defined stoichiometries and crystal structures) have been proposed as methods to overcome the aforementioned challenges with Si. However, nanostructured electrodes are difficult to synthesize at commercial scales and can lead to increased amounts of electrolyte decomposition due to the increased surface area. Intermetallics use additional metals that are not electrochemically active; thus, they act as conductive buffers that stabilize the structure and regulate the overall volume expansion of the anode. However, capacity fade and structural destruction are still observed over time due to the two-phase coexistence of Li-rich, and Li-poor phases during electrochemical cycling, where accumulated strains at the phase boundary lead to the mechanical pulverization of the active material. Thus, different approaches are required to address these issues.

This work explores a novel approach in using Si-based metallic glasses (Si-MG). Metallic glasses are amorphous alloys that are used in a variety of applications because of their unique properties, including high hardness and chemical inertness. Si-MG is an attractive category of materials for LIB due to its homogeneously distributed Si content that can eliminate the two-phase coexistence and materials pulverization through solid-solution alloying during electrochemical cycling. Thus, in comparison to polycrystalline intermetallic compounds, they present the advantage of lacking phase boundaries. Additionally, metallic glasses are known to simultaneously have high strength and high toughness (which are generally exclusive), i.e., metallic glasses are expected to be more resistant to pulverization. Multi-component Si-MGs can also provide a pathway to address the major issues associated with Si-based electrodes by carefully selecting the elements to be introduced. First, a proper choice of Li-inert element can become a buffer or reduce the magnitude of volume change during Li alloying/dealloying, which is the source of electrode-scale mechanical instability. Second, the use of elements that favor the formation of stable SEI (e.g., Ni) may tune the SEI on Si-MG to achieve full passivation.

Amorphicity and lack of phase separation are thus pivotal to improve the cycling stabilities of these new anodes. Previous attempts to produce amorphous thin films have only been demonstrated by sputtered deposition.[1,2,3] However, the cooling rate of the sputtering process is often not fast enough to enable the deposition of a truly amorphous material. Additionally, the resulting electrodes typically have thin-film geometry with thicknesses on the order of hundreds of nanometers. These disadvantages become barriers to the exploration of Si-MGs as practical LIB negative electrodes. This quarter, we successfully developed a Si-MG

($Al_{64}Si_{25}Mn_{11}$ at. %) using a splat quenching system. The splat quencher system enables extremely rapid quenching of the metal alloy melt, preventing the long-range reorganization of the atoms, and thus, the formation of alloys with an amorphous structure. The investigation carried out to date shows that $Al_{64}Si_{25}Mn_{11}$ glass is electrochemically active and forms a stable solid-electrolyte interphase unlike elemental Si. Insights from this study provide properties desired in an SEI interface and can guide future SEI design rules for Si-based anodes. Our work supports meeting the Go/NoGo Q2 milestone on "production of tin-silicon alloys to be determined by the ability of the alloys to be prepared in 1g quantities and a demonstration that the alloys exhibit greater cyclic life than the pure metals alone."

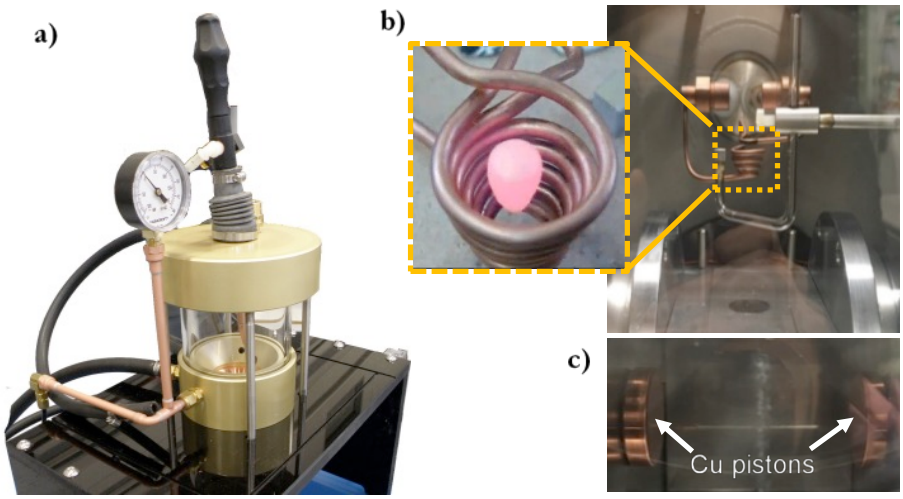

Figure 1. Photographs of the arc-melter and the splat cooling system. a) The parent $Al_{64}Si_{25}Mn_{11}$ alloy is fabricated by arc-melting Al, Si, and Mn powders. b) The parent alloy is liquified by the induction levitation technique, and c) the two copper pistons splat cool the melt at a rate of ~10^5–10^6 K/s.

Results

Materials synthesis and characterization

Metallic glasses are amorphous alloys produced from rapid cooling of a liquid melt to suppress the nucleation and growth of the crystalline phase. These rapid cooling rates can be achieved by several techniques including sputtering, mechanical milling, melt spinning, and splat cooling.[4] Splat cooling is advantageous because practical sample sizes can be synthesized and high cooling rates can be achieved.[5] A splat-cooling system (SCS) heats an alloy inductively through the levitation melting technique. In the levitation melting technique, an alternating high-current is applied through a levitation copper coil. The alternating current generates a high-frequency electromagnetic field, which produces the eddy current in the alloy. The eddy current plays two important roles: i) melting of the alloy by induction heating (typically above 1000 ºC), and ii) generation of electromagnetic body force, which makes the molten droplet to levitate by balancing the gravimetric force. This implies that the technique enforces at least one of the alloy components to have a ferromagnetic property for the electromagnetic levitation. After sufficient melting and homogenizing of an alloy, the levitation force is removed by stopping the application of the alternating current. Subsequently, the molten metal is dropped at free fall, which is captured by a laser detection module. The laser detection activates the high-speed motion of two copper pistons to "splat" the molten droplet. This process quickly quenches molten metals using cold metal surfaces at the cooling rate ranging from 10^5 to 10^8 Ks^{-1}. The entire synthesis is conducted in a high-purity Ar-filled environment, which allows minimal contamination of the alloy. A further advantage of this technique is that the precursor materials are fully converted into products during the splat quenching process, with no loss in the yield of conversion to amorphous glasses. At present, the heating and cooling rates have

been optimized to handle 20 mg of Si-MG per splat, making possible the process of production of 1-g quantity, albeit this requires multiple splats (50, at least). In the future, these process parameters will be optimized to increase the amount of raw materials processed per each splat, to achieve the production of 1 g of anode material in fewer steps. This will require adjustment of the heating current and velocity of the Cu piston to achieve adequate cooling rates.

Among all Si-MG, Al-Si-X (X = Cr, Ni, Fe, Mn) alloys are of particular interest because they have good glass-forming ability, and large composition ranges can be fabricated through economical techniques.[Error! Bookmark not defined.] Manganese is chosen as the third element due to its lower melting point and low cost. $Al_{64}Si_{25}Mn_{11}$ glass is prepared by rapidly cooling a liquid metal melt of a parent alloy using a SCS. The parent alloy, which has the same composition as the glass ($Al_{64}Si_{25}Mn_{11}$), was prepared by melting stoichiometric amounts of Al, Si, and Mn powder in an arc melter under Ar (Fig. 1a). The parent alloy was then melted at ~1100 ºC in the SCS through an induction levitation technique (Fig. 1b) and cooled by copper pistons at the rate of 10^5–10^8 K/s (Fig. 1c). The crystallinities of the parent alloy and the resulted rapid-cooled glass are measured by X-ray diffraction (XRD) (Fig. 2a). The parent alloy consists of three phases: crystalline Si (*Fd-3m*, JCPD No. 00-003-0549), Al (*Fm-3m*, JCPD No. 00-001-1179), and intermetallic $Al_{4.01}MnSi_{0.74}$ (*Pm-3*, 01-087-0528). After splat cooling, all crystalline peaks resolved into two broad bands at 20º and 42º, which suggests that the resulting material has an amorphous structure. The amorphicity of the glass is further confirmed by differential scanning calorimetry (DSC). The DSC curve (Fig. 2b) shows clear exothermic peaks, related to the crystallization process that the amorphous splat-quenched materials undergo at around 300 ºC. Thus, these peaks correspond to the crystallization temperature, T_c, of the metallic glass. This crystallization is confirmed by XRD (Fig. 2c); the amorphous XRD pattern (the two broad humps) turn into sharp peaks, indicating that the glass becomes a crystalline material after the DSC test.

The as-synthesized metallic glass is also analyzed using scanning electron microscopy (SEM) and transmission electron microscopy (TEM). The SEM image of the metallic glass (Fig. 3a) shows dense and smooth surface topography in comparison to the Si thin-film model electrode counterpart prepared by sputter deposition (Fig. 3b). The TEM images and the corresponding selected-area electron diffraction (SAED) patterns show that the metallic glass predominantly has an amorphous phase (Fig. 3c). We conducted extensive TEM imaging and discovered that the only regions of non-amorphicity are rare and isolated spots, with a diameter of about 4 nm maximum (yellow square in Fig. 3d).

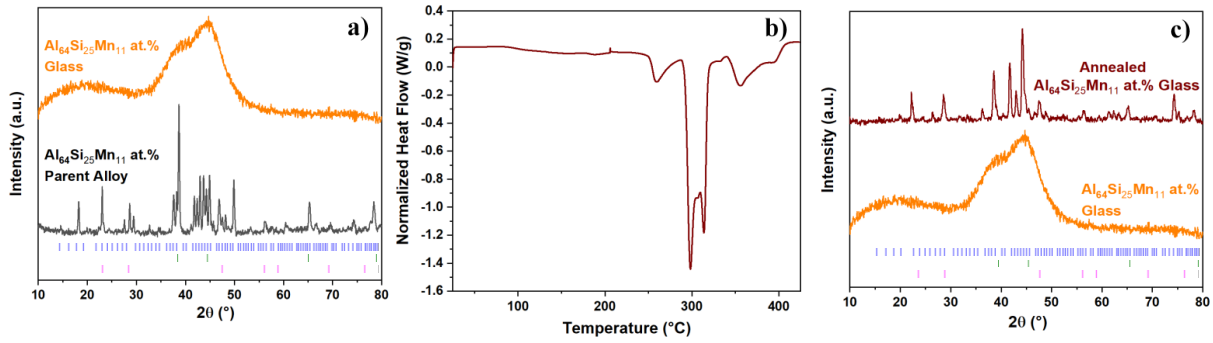

Figure 2. a) Powder XRD of the parent $Al_{64}Si_{25}Mn_{11}$ parent alloy (gray) and the amorphous analogue after rapid quenching (orange). b) DSC curve of $Al_{64}Si_{25}Mn_{11}$ glass. c) XRD of $Al_{64}Si_{25}Mn_{11}$ glass after DSC (red) in comparison to the pristine amorphous $Al_{64}Si_{25}Mn_{11}$ alloy (orange).

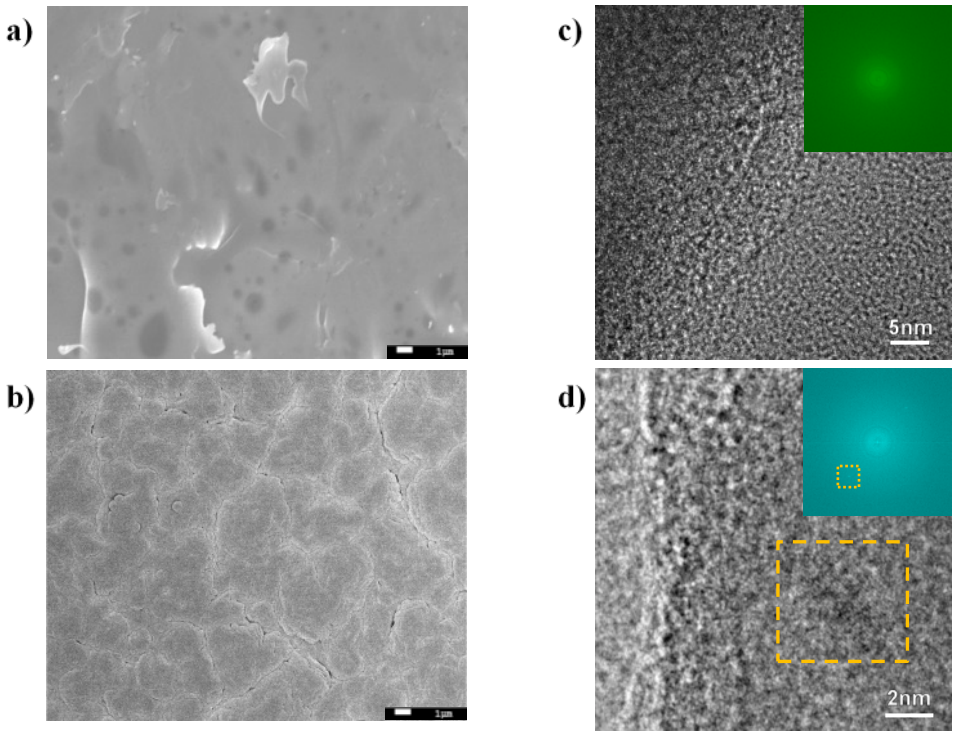

Figure 3. a) An SEM image of $Al_{64}Si_{25}Mn_{11}$ glass. b) An SEM image of Si thin-film model electrode. c) High-resolution TEM image of $Al_{64}Si_{25}Mn_{11}$ glass showing amorphous structure. d) High-resolution TEM image of $Al_{64}Si_{25}Mn_{11}$ glass showing a nanocrystal grain with the size of ~4 nm (highlighted by a yellow box). The insets in c,d) show the corresponding SAED.

Electrochemistry

To investigate the electrochemical performance, the $Al_{64}Si_{25}Mn_{11}$ glasses are cycled in half-cells (three-electrode Swagelok cells) against Li. A foil form (~2–4 μm in thickness, ~6 mm in diameter) of metallic glass is cycled instead of fabricating composite electrodes to avoid any electrochemical contribution from the carbon, binder and the current collector. Figure 4a shows the cyclic voltammogram (CV) of $Al_{64}Si_{25}Mn_{11}$ glass cycled at 0.1 mV/s in 1.2 M $LiPF_6$ EC: EMC (3:7 wt.%) between 0.005 V and 1.5 V vs. Li/Li^+. Typically, Li alloys with Al at ~0.23 V vs. Li/Li^+ to form LiAl and alloys with amorphous Si at ~0.18 V and 0.06 V vs. Li/Li^+ to form Li_xSi.[6,7] However, the presented CV shows a sharp peak at 0.005V during the first lithiation process. The sharp peak can be attributed to a large overpotential caused by slow diffusion of Li in the metallic glass. The slow diffusion originates from the lack of crystal structure and densely packed atoms found in metallic glass. During delithiation, a broad asymmetric peak can be observed at ~0.3 V. For comparison, the dealloying reactions of Li from LiAl is 0.43 V vs. Li/Li^+ and Li_xSi is 0.3 and 0.5 V vs. Li/Li^+. We thus believe that this broad feature corresponds to the delithiation process from the metallic glass. In the subsequent cycles, the reduction peak broadens as Li^+ diffusion is improved and more material is being activated.

Figure 4b shows the potential profiles of the $Al_{64}Si_{25}Mn_{11}$ glasses during three galvanostatic cycles. A low current (~50 μA) is selected, in consideration of the slow kinetics observed in the CV results. The potential profiles agree with the redox signatures shown in the CV. A plateau is observed at 0.005 V during the first lithiation, which transforms to a more inclined slope in the subsequent cycles, mirroring the broadening of the reduction peak seen in the CV. During the first cycle, a capacity of 1,094 mAh/g is obtained with 57% coulombic efficiency (CE). The capacity of the second cycle is lower (627 mAh/g, 87% CE) due to the irreversibility in the previous cycle. As Li diffusion through the metallic glass improves, higher capacity is observed again in the third cycle (1,024 mAh/g, 81% CE). It should be noted that it is likely the entire mass of the glass does not participate during the galvanostatic cycling because of a relatively thick foil-shaped geometry; the actual specific capacity is expected to be higher than the measured values. Furthermore, the high content of Al, notoriously showing large irreversible capacity, will contribute to reduce the capacity. This shortcoming will be overcome in future studies by reducing the amount of aluminum or completely replacing this element.

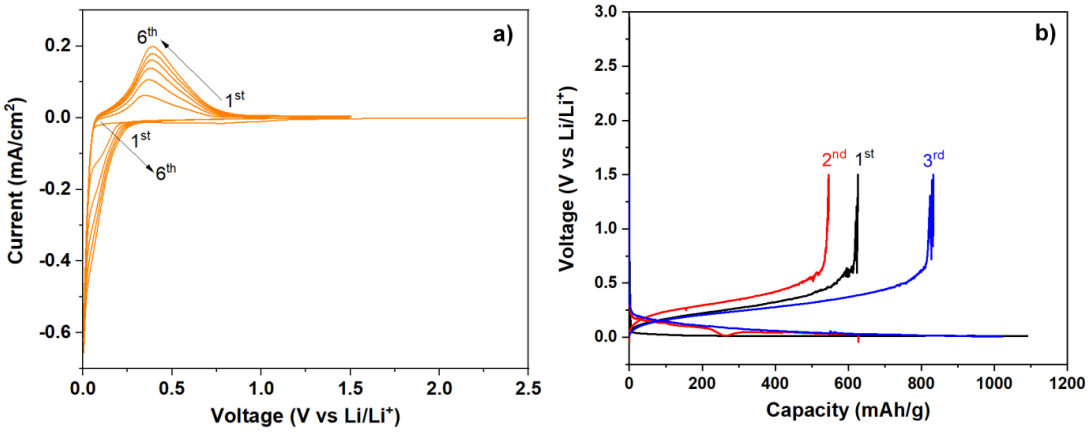

Figure 4. a) Cyclic voltammogram of $Al_{64}Si_{25}Mn_{11}$ at.% glass at 0.1 mV/s, and b) galvanostatic cycling curves of $Al_{64}Si_{25}Mn_{11}$ glass at 50 μA in 1.2 M $LiPF_6$ EC: EMC (7wt.%) from 0.005 V to 1.5 V vs. Li/Li^+, respectively.

Alloying Mechanisms

To maintain structural integrity and avoid pulverization, the glass should remain amorphous throughout electrochemical cycling, which minimizes lattice mismatch. In this regard, it is essential to investigate whether $Al_{64}Si_{25}Mn_{11}$ glass phase separates into crystalline phases as it alloys with Li. *Ex-situ* XRD (Fig. 5a) is performed on $Al_{64}Si_{25}Mn_{11}$ glass at the lithiated (0.005 V) and delithiated (1.5 V) states to investigate the possible phase change during cycling. At the lithiated state, a broad band emerged at higher 2θ, at 62°, indicating a formation of a new amorphous phase. The broad band observed at ~42°, which also presents in the XRD pattern of the as-synthesized, can be explained by incomplete lithiation of the glass foil. The additional peak visible in the XRD pattern of the lithiated stage is attributed to LiF and Li_2CO_3 electrolyte decomposition products, as films were only dried but not washed off prior to the XRD measurements. At the delithiated state, the intensity of the broad peak at $2\theta=62°$decreased. The peak is not expected to fully disappear based on the irreversibility observed in the CV and galvanostatic cycling curves. The increased intensity of the $2\theta=42°$ peak and the reemergence of the broad band at lower 2θ indicates the formation of the original $Al_{64}Si_{25}Mn_{11}$ phase observed in the pristine samples. Most importantly, no crystalline phases were observed, suggesting $Al_{64}Si_{25}Mn_{11}$ glass remains amorphous throughout the cycling. For further confirmation, *ex-situ* TEM analysis was conducted on the lithiated glass (Fig. 5b). The high-resolution TEM and the SAED pattern of the lithiated glass show no sign of a crystalline phase, which agrees with the results from the *ex-situ* XRD measurements.

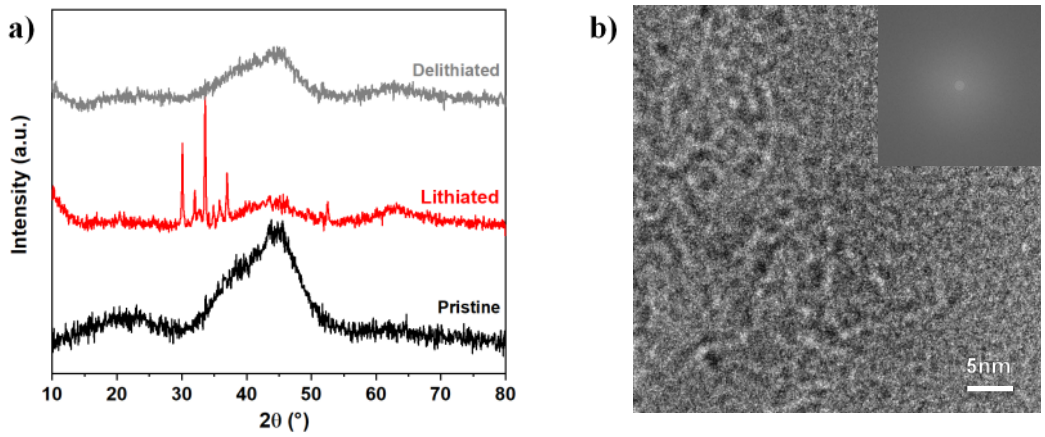

Figure 5. a) *Ex-situ* XRD of the $Al_{64}Si_{25}Mn_{11}$ glass at the pristine state (black), lithiated state (red), and delithiated state (gray). b) *Ex-situ* TEM of the $Al_{64}Si_{25}Mn_{11}$ glass at the lithiated state.

Solid-Electrolyte Interphase Study

Electrochemical impedance spectroscopy (EIS) was measured after every CV to monitor the stability of the solid-electrolyte interphase (SEI) of the 500-nm Si thin-film model electrode (Fig. 6a-b) and $Al_{64}Si_{25}Mn_{11}$ glass (Fig. 6c-d). The total resistance, which includes the electrode, electrolyte, and interfacial impedance of both $Al_{64}Si_{25}Mn_{11}$ glass and Si model electrode were obtained from their respective Nyquist plots (Fig. 6e). The equivalent-circuit model used to fit our data is shown in the inset of Fig. 6e. The total resistance of the Si model electrode increased significantly (a factor of four) after 10 cycles as shown in Fig. 6e. On the contrary, the total electrical resistance of $Al_{64}Si_{25}Mn_{11}$ glass only increased slightly, suggesting that the SEI formed on the $Al_{64}Si_{25}Mn_{11}$ glass is stable. The electrolyte did not continuously degrade throughout cycling to form more SEI.

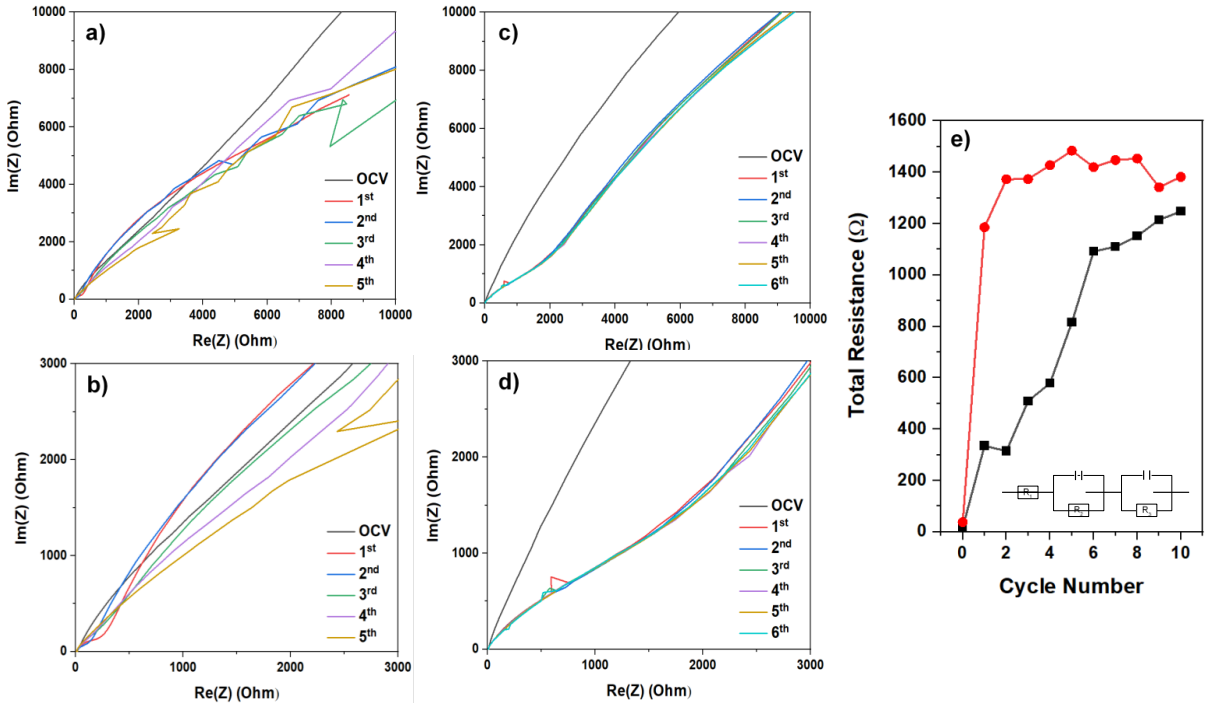

Figure 6. SEM images of 500-nm Si model electrodes a) before and b) after 5 cycles. $Al_{64}Si_{25}Mn_{11}$ glass c) before and d) after 5 cycles. **e)** The total-resistance evolutions of the metallic glass and the Si model electrode with increasing cycle number.

The improved interfacial stability of $Al_{64}Si_{25}Mn_{11}$ glass can also be demonstrated from the current density at the SEI formation potential. Figure 7a-b shows the CV curves of the 500-nm Si model electrode, $Al_{64}Si_{25}Mn_{11}$ glass, and a Cu foil cycled in 1.2 M EC:EMC (3:7 wt.%) during the first cycle. The CV curves show a much lower current density for $Al_{64}Si_{25}Mn_{11}$ glass at ~0.5–0.6 V (the SEI formation potential) compared to the 500-nm Si thin-film case, which suggests that the glass is more chemically inert and reduces less electrolyte. The current density of the glass near the SEI formation potential is comparable to Cu, which is known to form a

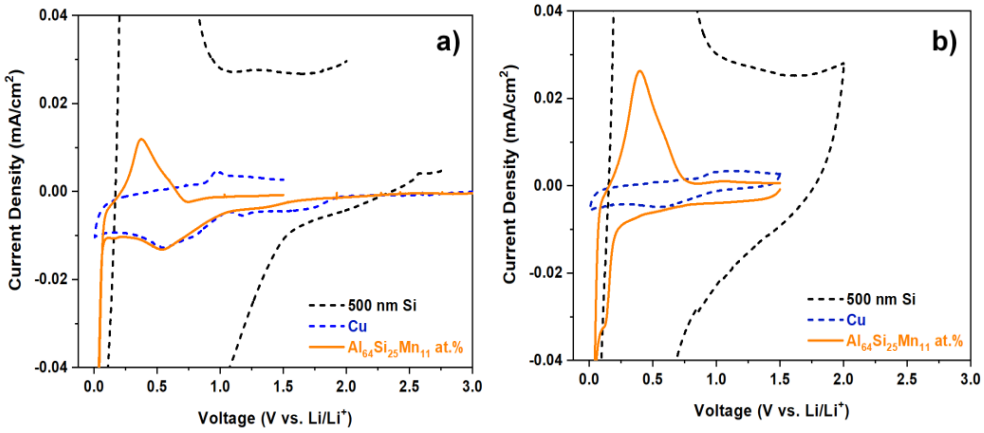

Figure 7. Cyclic voltamogram of 500 nm Si model electrodes (dash/black), Cu foil (dash/blue), and $Al_{64}Si_{25}Mn_{11}$ glass (orange) during the **a)** first and **b)** second cycle.

stable SEI. During the second cycle, the peak observed at ~0.5–0.6 V on the first cycle disappeared, as expected. The current density remained low for the glass and is still comparable to Cu.

Conclusions and Outlook

In summary, Si-based metallic glass, $Al_{64}Si_{25}Mn_{11}$, was successfully synthesized through a splat cooling system by rapidly cooling the liquid melt of $Al_{64}Si_{25}Mn_{11}$ alloy and suppressing the nucleation and growth of the crystalline phase. $Al_{64}Si_{25}Mn_{11}$ glass exhibits good specific capacity and has demonstrated superior interfacial stability in comparison to elemental Si. EIS shows a drastic increase in the total resistance of the 500-nm Si electrode after 10 cycles. On the contrary, the total resistance of the glass remained almost constant, suggesting the formation of a stable SEI layer. These findings strongly support the validity of our approach: a stabilization of electrode/electrolyte interface by using amorphous multi-component metallic glass as an anode material.

As future investigations for the $Al_{64}Si_{25}Mn_{11}$ alloy, we plan to screen the splat quenching parameters such as the different temperature to which the molten-alloy droplet is brought up during the electromagnetic levitation and the time for which the alloy is kept levitated (time that the alloy is kept in the liquid form prior to quenching it). Additionally, we plan to replace Mn by other elements such as Ni or Fe to improve the SEI stability, cost efficiency, Li alloying kinetics, and to avoid possible Mn dissolution into the electrolyte. Furthermore, we will increase the Si content in the metallic glass to minimize the Li trapping by Al. Compositions that present the right magnetic properties to sustain electromagnetic levitation will be investigated by splat quenching. For compositions that are not able to sustain this type of levitation, additional cooling methods will be explored, such as pulsed laser cooling.

In terms of future characterization, we plan to carry out a thorough investigation of the SEI formed on the surface of these bulk metallic glasses to unpin the qualitative and quantitative differences in comparison to the SEI formed on Si. In addition to traditional post-mortem characterization methods (such as SEM, Raman, FT-IR, and XPS), we will make use of the nano FT-IR method to further characterize the evolution of the SEI on the BMGs as a function of cycling.

In terms of studying the mechanical stabilities of BMG, we plan to perform prolonged cycling on the bulk materials to assess the coulombic efficiency and presence of cracking after extensive electrochemical activity. Potentially, the material could be rendered in nanoparticle form, and additional characterization of the resulting electrodes are envisaged.

These future directions are expected to help optimize the specific capacity, kinetics, interfacial stability, and cycle life of amorphous glasses, which will vastly increase the potential of their commercial applications as next-generation anode materials.

References

1. Beaulieu, L. Y., Hewitt, K. C., Turner, R. L., Bonakdarpour, A., Abdo, A. A., Christensen, L., Eberman, K. W., Krause, L. J., Dahn, J. R. The Electrochemical Reaction of Li with Amorphous Si-Sn Alloys. Journal of The Electrochemical Society 150, A149-A156 (2003).

2. Hatchard, T. D., Dahn, J. R. Study of the Electrochemical Performance of Sputtered Si1-xSnx Films. Journal of The Electrochemical Society 151, A1628-A1635 (2004).

3. Fleischauer, M. D., Dahn, J. R. Combinatorial Investigation of the Si-Al-Mn System for Li-Ion Battery Applications. Journal of The Electrochemical Society 151, A1216-A1221 (2004).

4. Khan, M. M., Nemati, A., Rahman, Z. U., Shah, U. H., Asgar, H., Haider W. Recent Advances in Bulk Metallic Glasses and Their Applications: A Review. Critical Reviews in Solid State and Materials Sciences 43, 233-268 (2018).

5. Nair, B., Priyadarshini, B. G. Process, Structure, Property and Applications of Metallic Glasses. AIMS Materials Science 3, 1022-1053 (2016).

6. Hamon, Y., Brousse, T., Housse, F., Topart, P., Buvat, P., Schleich, D. M. Aluminum Negative Electrodes in Lithium Ion Batteries. Journal of Power Sources 97-97, 185-187 (2001).

7. Jerliu, B., Huger, E., Dorrer, L., Seidlhofer, B. K., Steitz, R., Horisberger M., Schmit H., Lithium Insertion into Silicon Electrode Studied by Cyclic Voltammetry and Operando Neutron Reflectometry. Physical Chemistry Chemical Physics 20, 23480-23491 (2018)

Next-Generation Anodes for Lithium-Ion Batteries

Greg Pach, Fernando Urias, Nathan Neale (NREL)

Background

In Q1 FY20, we began exploring an alternative methodology based on nonthermal plasma synthesis to fabricate tin-silicon alloys to complement work at LBNL using the SPLAT synthesis method for these active materials. Nonthermal plasma synthesis provides a unique pathway for materials synthesis in which the non-equilibrium plasma process can allow for the formation of alloyed nanoparticles (NPs) that are metastable (i.e., unstable thermodynamically), such as SiSn alloys. Although Sn has an intrinsically lower lithium capacity than Si, the presence of Sn could help boost the NP conductivity within composite anodes while additionally helping to form a more stable SEI layer. Furthermore, these group IV alloys can also allow us to study more fundamental material properties such as the effect of NP strain caused by the larger size of Sn atoms relative to Si during lithiation and delithiation.

Results

In Q2 FY20, we made great strides toward these ends and have demonstrated incorporation of small amounts <10 at. % of Sn into SiSn alloys using the nonthermal plasma approach. Tin incorporation is confirmed using a suite of chemical and structural characterization techniques including diffuse reflectance infrared Fourier transform spectroscopy (DRIFTS), X-ray diffraction (XRD), transmission electron microscopy (TEM), and energy-dispersive X-ray spectroscopy (EDS) mapping. We have also incorporated these materials in composite lithium-ion battery (LIB) anodes and studied their cycling performance in a half-cell architecture for 50 cycles. Along with work from LBNL, these results help meet the Go/NoGo Q2 Milestone on “production of tin-silicon alloys to be determined by the ability of the alloys to be prepared in 1g quantities and a demonstration that the alloys exhibit greater cyclic life than the pure metals alone.”

The nonthermal plasma synthesis process for production of SiSn alloy NPs involves the flow of precursor gases of SiH_4, $Sn(CH_3)_4$, Ar, and H_2 through a 1"-outer-diameter reactor tube in which a plasma is produced via use of a capacitively coupled radio-frequency electrode delivering ~100 W of forward power. The final NP alloy composition is therefore based on the gaseous precursor ratio of SiH_4 to $Sn(CH_3)_4$. We have found that to produce an alloyed phase, the pressure needs to be kept below 4 Torr with high excess H_2 flow; otherwise, metallic Sn precipitates from the plasma. Figure 1a shows the DRIFTS spectra from three different NP samples: pure intrinsic Si, 5 at. % Sn ($Si_{0.95}Sn_{0.05}$), and 10 at. % Sn ($Si_{0.9}Sn_{0.1}$). The absorption feature at 1,790 cm^{-1} is attributed to $*SnH_x$ stretching vibrations, where the * denotes a surface Sn atom, and it is noticeably absent in the pure Si

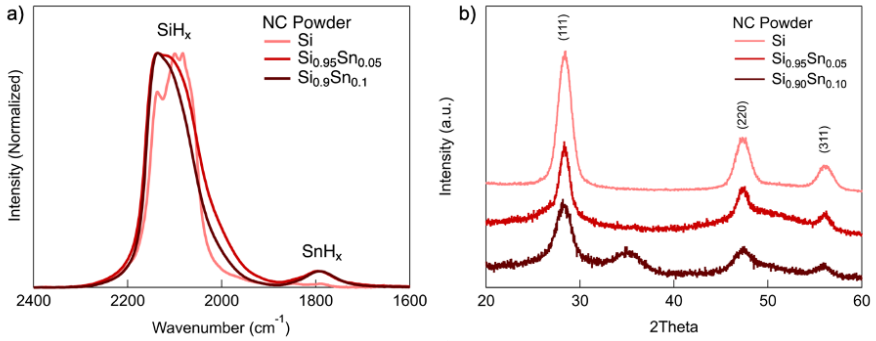

Figure 1. a) DRIFTS spectra for pure Si, 5 atomic % Sn ($Si_{0.95}Sn_{0.05}$), and 10 atomic % Sn ($Si_{0.9}Sn_{0.1}$) NPs. SiSn alloys show a peak at 1,790 cm^{-1} characteristic of SnH_x. b) XRD spectra for Si, $Si_{0.95}Sn_{0.05}$, and $Si_{0.9}Sn_{0.1}$ NPs. The well-defined peaks point to formation of a crystalline alloyed material.

NP sample. Additionally, the $*SiH_x$ stretching region (2,000–2,200 cm^{-1}) for the alloyed NPs becomes less well-defined, with a broader peak that has a maximum intensity at higher energies and a lower-energy tail extending below 2,000 cm^{-1}. The shift in peak maximum intensity toward higher wavenumbers suggests a higher proporotion of the silicon trihydride group $*SiH_3$, and, combined with the lower-energy tail, it is characteristic of an amorphous, more highly strained surface resulting from Sn incorporation into these alloyed NPs. Figure 1b shows XRD spectra of the same set of samples. The well-defined peaks corresponding to the (111), (220), and (311) facets point to mostly crystalline NPs; however, the elongated aspect of the (220) peak is indicative of some amorphous character. The peak exhibited at ~35 degrees 2θ in the $Si_{0.9}Sn_{0.1}$ is still unknown to us; however, we believe that it may be indicative of a SiSn alloy phase.

Characterization on SiSn alloys was also done using TEM and EDS, allowing us to further examine the crystalline and elemental composition of the SiSn NPs. Figure 2 shows a TEM image of a cluster of $Si_{0.9}Sn_{0.1}$ NPs in which the NPs appear highly monodispersed. The right-hand side of Fig. 2 displays EDS data. The bottom-left and bottom-right images map Si and Sn, respectively, within the NP sample. Importantly, the Sn signal is observed to track the Si signal, which provides evidence of alloy formation, whereas Sn hotspots would be indicative of phase segregation or pure-phase Sn particles. From the EDS, the Si:Sn ratio is calculated to be 85:15 at %, which compares well with our Si:Sn 90:10 gaseous precursor ratio.

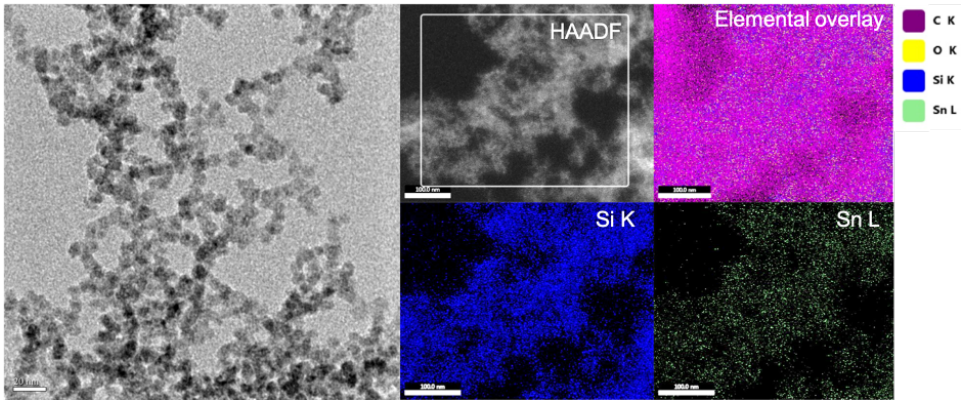

Figure 2. Left: TEM image of a cluster of $Si_{0.9}Sn_{0.1}$ NPs. Scale bar is 20 nm. Right: EDS elemental analysis of the same NP sample shown on the left. Top left shows the HAADF image while the bottom left and bottom right show Si and Sn mapping, respectively. The Si and Sn are seen to track each other, showing evidence of alloy formation. The top right shows the elemental-map overlay including C, O, Si, and Sn.

These SiSn alloy NPs were constructed into composite anodes using our air-free methodology slurry and electrode fabrication processes described in other SEISta reports. In brief, two different compositions and sizes—7.4-nm $Si_{0.95}Sn_{0.05}$ and 5.1-nm $Si_{0.9}Sn_{0.1}$. SiSn NPs—were first functionalized with N-methyl-2-pyrrolidone (NMP) by heating NPs in purified NMP in the presence of catalytic amounts of the radical initiator 1,1′-azobis(cyclohexanecarbonitrile). Slurries were prepared using in-house purified polyacrylic acid (PAA) binder, dried Timcal C65 conductive carbon, and purified NMP. SiSn NPs and C65 conductive carbon were added at a 1:1 mass ratio yielding anodes of ~33 wt % active material. Coin cells were then fabricated using a Li metal cathode and Gen2 electrolyte with 10 wt % FEC (Gen2F). Cells were cycled at C/20 for three formation cycles and then C/5 for all additional cycles.

Figure 3 displays plots of the electrochemical cycling data for the SiSn NP composite anodes. Specific capacity is quite good for both alloy anodes, which retain ~92% of their original (4^{th}-cycle) capacity after 50 cycles. This value compares very well with that of pure intrinsic Si@NMP NP-based anodes, which exhibit just 72% of their 4^{th}-cycle specific capacity (data not shown). Particularly noteworthy is the rapid stabilization of the coulombic efficiency (CE) in the first four cycles. Anodes made using $Si_{0.95}Sn_{0.05}$ NPs reach their maximum CE on the 5^{th} cycle, whereas $Si_{0.95}Sn_{0.05}$ NP anodes are within 0.1% of their maximum CE by the 5^{th} cycle (i.e., essentially stabilized by the 5^{th} cycle). As part of our durability study, we have come up with a new metric for evaluating half-cell and full-cell data that can be used to quantify cycle life of anodes by plotting $CE_{cycle\ n}$ vs. cycle number, i.e., the cumulative CE over all cycles. For these SiSn-alloy NP-based anodes, the cumulative CE over all cycles is just below 50% after 50 cycles, which is a huge improvement compared with that of pure Si anodes with the same NMP surface functionalization (~10%, data not shown).

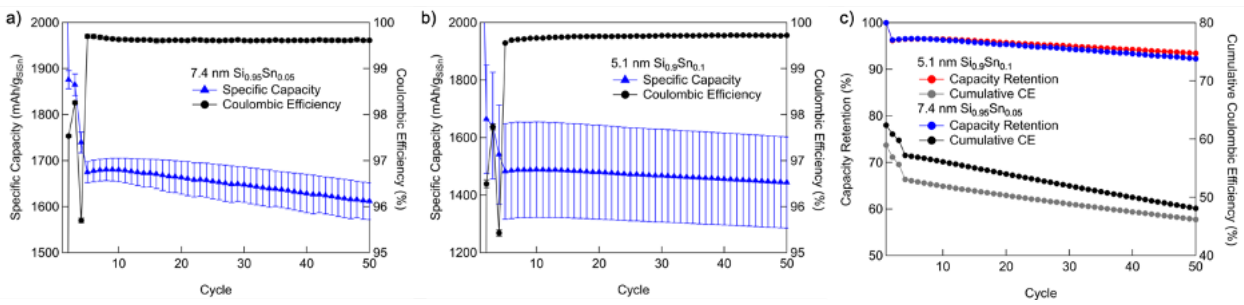

Figure 3. Cycling performance for SiSn composite anodes. Specific capacity and coulombic efficiency over 50 cycles (3 forming cycles at C/20 and 47 cycles at C/5) are shown for a) 7.4-nm $Si_{0.95}Sn_{0.05}$, and b) 5.1-nm $Si_{0.9}Sn_{0.1}$-based NP anodes. Error bars are a 1-sigma deviation from a set of three anodes. c) Capacity retention—with respect to the 4th cycle—and cumulative coulombic efficiency over 50 cycles including the forming cycles for the electrodes.

Finally, Figure 4 shows differential capacity curves for the first three formation cycles at C/20 for SiSn NP composite anodes. Both plots show characteristic features during the first lithiation cycle at 1.2, 0.9, and 0.1 V vs Li^+/Li that are attributed to SiH_x reduction, SEI formation, and crystalline Si lithiation, respectively. Subsequent lithiation cycles show features at 0.21 and 0.07 V vs Li^+/Li that are indicative of amorphous Si lithiation as expected for the 2nd cycle and beyond. Interestingly, both the 5.1-nm $Si_{0.9}Sn_{0.1}$ and the 7.4-nm $Si_{0.95}Sn_{0.05}$ anodes exhibit a reduction feature at ~0.45 V vs Li^+/Li during lithiation and a corresponding oxidative process as a shoulder on the delithiation peak centered at ~0.7 V vs Li^+/Li. In previous SEISta reports, we have discussed this feature occurring with increasing intensity with decreasing Si NP size, and we believe it is related to surface strain at smaller NP sizes that may enhance Li-ion diffusion through the Si|SEI|electrolyte interface. Here, this feature appears to be about the same intensity for anodes made from both the 5.1-nm $Si_{0.9}Sn_{0.1}$ and the 7.4-nm $Si_{0.95}Sn_{0.05}$ NPs, and thus, it appears to be independent of size. We posit that the size independence of this feature for both 5.1-nm and 7.4-nm SiSn NP-based anodes is evidence of a strain-related effect due to Sn incorporation.

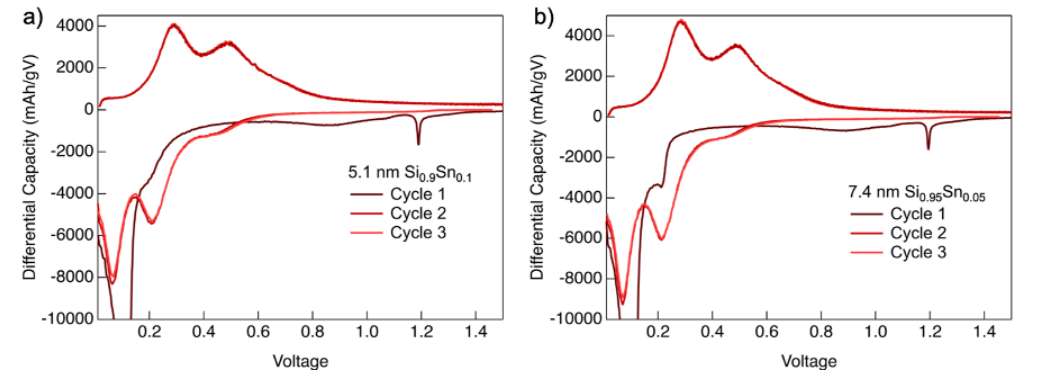

Figure 4. Differential capacity plots for SiSn composite anodes. Differential capacity is shown for the first three cycles (C/20) for a) 7.4-nm $Si_{0.95}Sn_{0.05}$ and b) 5.1-nm $Si_{0.9}Sn_{0.1}$ anodes.

Conclusions

The nonthermal plasma synthesis method was used successfully to produce SiSn alloy NPs. SiSn NPs were incorporated into composite anodes using our air-free process and demonstrate excellent capacity retention and cumulative coulombic efficiency over 50 cycles. Future work will explore the origin of the redox wave in the dQ/dV plots with respect to strain induced by Sn and by modifying our synthetic procedures to increase the SiSn NP size. Additionally, we plan to explore whether the surface chemistries that result in higher performance for intrinsic Si NP-based anodes also translate into better performance in SiSn-based composites.

Part 4: Influence of Carbon Dioxide on Si Anode Cycling

Gabriel Veith (ORNL), Emma Hopkins (ORNL), Ryan Pekarek (NREL), Steven Harvey (NREL), Chen Fang (LBNL), Gao Liu (LBNL), Caleb Stetson (NREL), Zoey Huey (NREL), Guang Yang (NREL), Baris Key (ANL), Xiang Li (ANL), Glenn Teeter (NREL), Sarah Frisco (NREL)

Background

The goal of this work was to "Have determined the affect that CO_2 has on the stability of SEI formation on model electrodes, but examining the changes in the nature of the SEI (XPS, FTIR/Raman, and quantitative electrochemical measurement) as a function of CO_2 concentration." To accomplish this, a team of scientists from multiple laboratories collaborated to evaluate the resulting SEI chemistry from pouch-cell-type batteries, with and without gaseous CO_2. The cells were built and cycled at ORNL using our standard GENII electrolyte with 50-nm amorphous silicon electrodes and lithium-metal counter electrodes with a Dreamweaver separator to ensure electrolyte wetting and CO_2 transport. Samples were sent to the partner laboratories for Fourier transform infrared spectroscopy (FTIR) [NREL], matrix-assisted laser desorption/ionization (MALDI) [LBNL], Raman [ORNL], X-ray photoelectron spectroscopy (XPS) [ORNL], time-of-flight secondary-ion mass spectrometry (TOF-SIMS) [NREL], nuclear magnetic resonance (NMR) [ANL], and scanning spreading resistance microscopy (SSRM) []NREL] analysis.

We found the following results:

1. The SEI chemistry changed significantly when using CO_2, resulting in an SEI layer that has significantly more inorganic component.
2. The irreversible capacity losses were constant regardless of the presence of CO_2.
3. Fabrication of the cells was important, and there is still an unresolved issue that we believe is due to air or water infiltration.
4. Air or moisture infiltration has a larger impact on cell performance than CO_2.

Results

As part of this set of experiments, we prepared multiple test cells cycled under the same conditions. These test cells involve the formation of pouch-cell-type batteries. The electrodes were 2"×2" in area. We used three pieces of Dreamweaver separator. This material was chosen because it wets extremely well with electrolyte (almost instantaneous); because of this wettability, we believe it will allow gas infiltration and transport. The cells were sealed in a glovebox under argon. Samples were removed to air and the CO_2 was dosed to the cell using a gas-tight syringe. Cells were stacked under a 500-g copper plate to provide stack pressure. The cells were cycled at a C/10 rate for 9.5 cycles (10 lithiations). The cycled cells were loaded into the glovebox and disassembled. Portions of the cells were washed with 2 mL of dimethyl carbonate (drop-wise addition) and dried under vacuum. Other parts were unwashed for MALDI or NMR experiments. The advantage of this approach is that all the characterization was performed on the same set of samples instead of samples made at different laboratories. We note that this is important for this work because the dosing process affects cycling.

Figure 1. Images of the Si electrode (left), Li electrode (center left), pouch cell being injected with electrolyte (center right), and pouch cell injected with CO_2 (right).

During the course of these experiments, we observed that dosing and cell preparation had a major influence on reproducibility. Figure 2 shows a collage of data collected for different cell fabrication and dosing protocols. As can be seen in these data, the pie charts show the average elemental composition for at least two samples measured by XPS, along with the cycling data. In Round 1, cells were sealed after bringing to air, with or without dosing with CO_2. Under this process, the XPS data looked the same (composition and cycling). In Round 2, the cells were sealed in a glovebox, then the leads were coated in epoxy because this was viewed as a source of gas leakage. In Round 3, the CO_2 gassing protocol was revised to use a gas-tight syringe to dose the samples with 2 mL of CO_2 through the smallest hole possible. As can be seen from the experiments in Round 2 and 3, the SEI compositions were similar whereas varying significantly from Round 1.

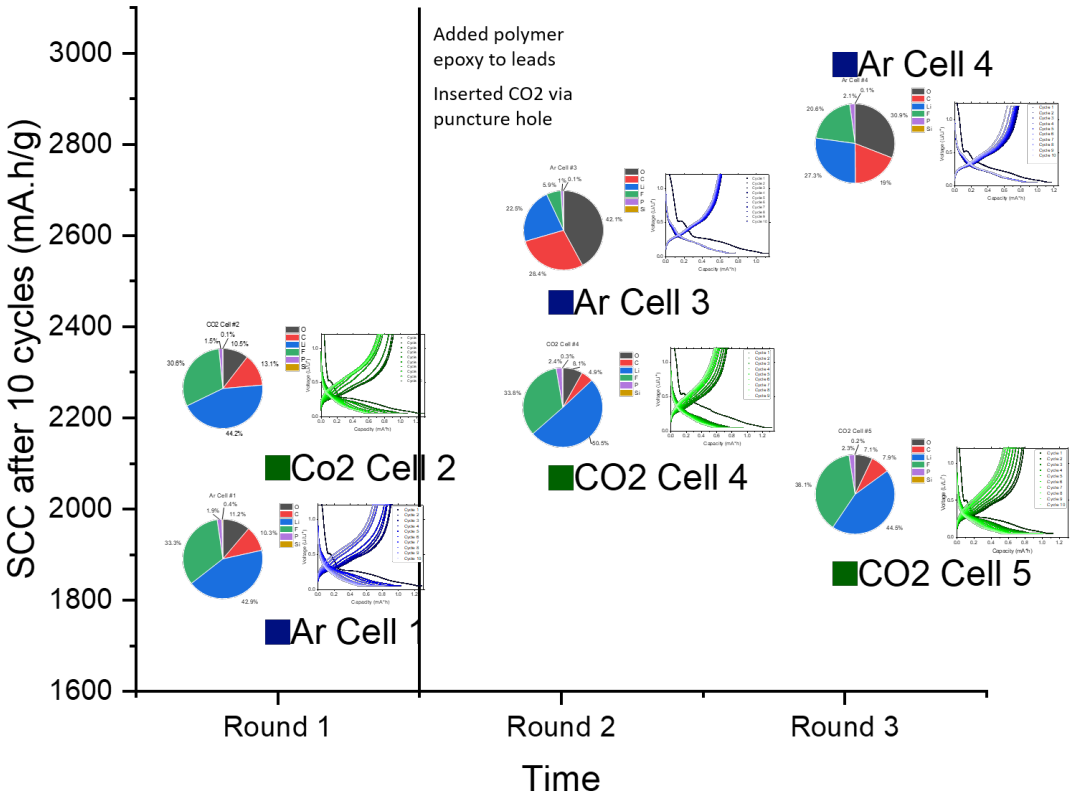

Figure 2. Collage of SEI capacity and capacity retention as a function of fabrication method. Left axis is the capacity retention after 10 lithiations for the standard 50-nm electrode.

From these data, it is clear that the SEI becomes more inorganic-like with the introduction of CO_2, as evident by the increase in F and Li content (green and blue data, respectively). Note that we use F as a marker for inorganic LiF-type SEI layers. In contrast, the SEI with Ar cells has higher concentrations of carbon (red) and oxygen (black). The higher concentrations of carbon and oxygen are consistent with a more "organic-like" SEI layer. Interestingly, these results mimic what was observed using neutron reflectivity data to follow the SEI formation with and without FEC. The FEC-containing electrolyte resulted in a more F-rich SEI whereas the FEC-free was more organic in nature. This points to the CO_2 promoting the inorganic SEI components. These same cells were shipped to the partner laboratories detailed above for further characterization. Note that we attempted Raman spectroscopy data collection, but had inconclusive results.

The second observation that is clear from the data is that the CO_2 has no apparent benefit to the cycling performance of the electrodes over a standard argon configuration. Figure 3 shows average cycling data collected for at least three cells, along with error bars for these measurements. The left data show the cells measured in argon, and the right data show cells dosed with CO_2. Both cells show large irreversible capacity losses with the first cycle and a slow but steady decline in capacity retention with further cycling. These data indicate that CO_2 is not the cure to an unstable SEI.

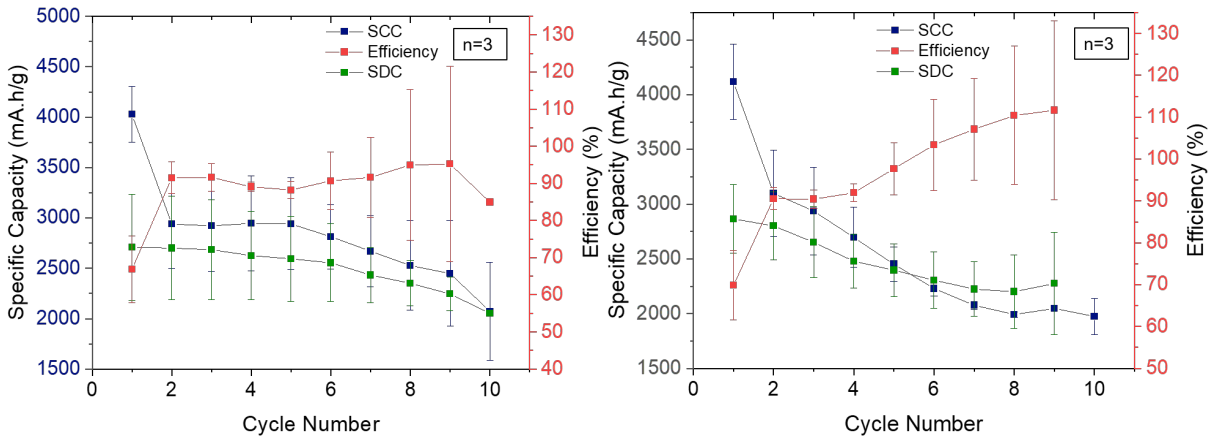

Figure 3. Average cycling data for cells cycled in argon (left) and CO_2 (right).

Figure 4 presents representative FTIR data collected for the samples in Round 3. As is clear from the Ar FTIR data, we see more organic Li-O-C species whereas the CO_2 sample (blue) shows a significantly different FTIR spectra consistent with the presence of LiF. Similarly, TOF-SIMS data collected on the samples (Fig. 5) showed a much higher concentration of F species on the surface, with lower C-O content for the cells dosed with CO_2.

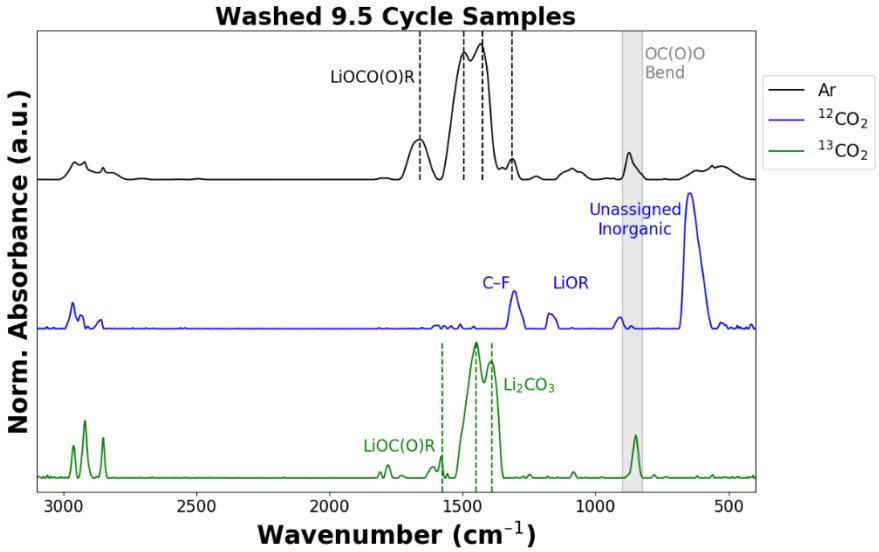

Figure 4. FTIR data collected for the washed electrodes with and without CO_2.

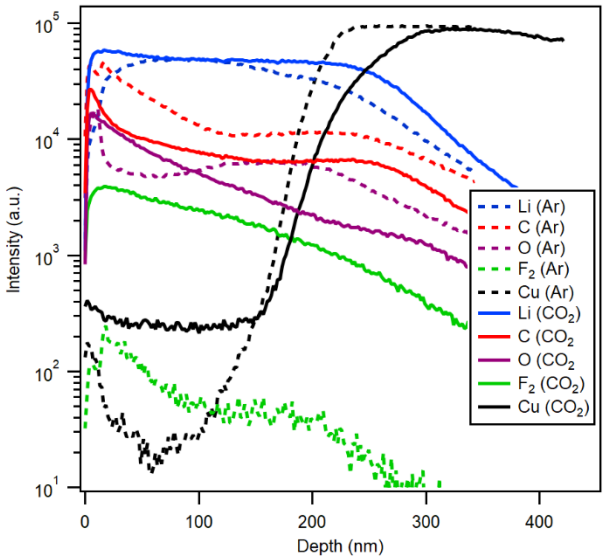

Figure 5. TOF-SIMS data collected for the washed electrodes with and without CO_2.

SSRM studies were performed on the washed SEI. Representative resistance data as a function of depth are presented in Fig. 6. These data show that the SEI for the cells made in the CO_2 was thinner and less resistive than the SEI made using electrolyte exposed to argon. Interestingly, this thinner SEI is consistent with the SEI measured on cells formed with FEC, which were more LiF-like.

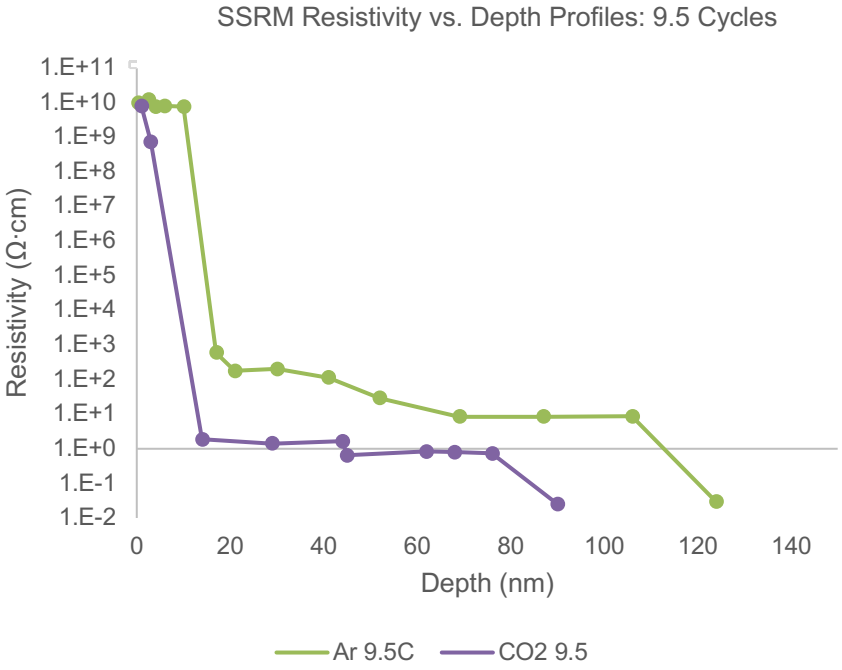

Figure 6. SSRM data showing the resistance of the insoluble part of the SEI as a function of depth.

Unwashed electrodes analysis

To explore the organic part of the SEI further, unwashed samples were subjected NMR, gradient wash, and MALDI experiments. Figure 7 shows representative data collected during the gradient washing process. In this work, progressively larger fractions of hexane are added to an ethyl acetate solution. The electrode is evaluated as a function of hexane:EA ratio. The hexane is a "less" aggressive solvent for removing SEI components whereas EA dissolves more carbonate and polymer species. After each wash, the electrode surface was probed with FTIR spectroscopy. These data show that the more aggressive wash removes increasingly more of the surface SEI. Furthermore, this wash removes more of the organic SEI components (1,400–1,000 cm^{-1} signals).

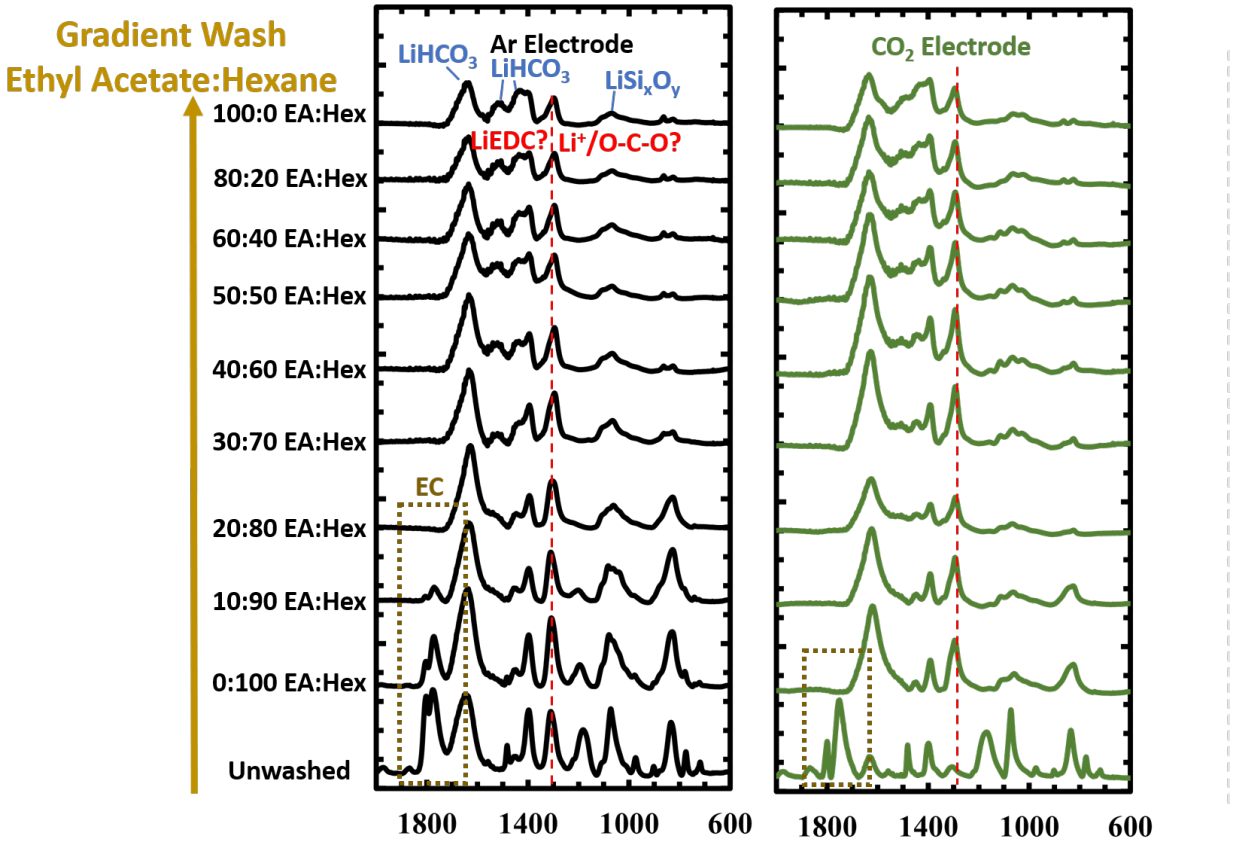

Figure 7. FTIR data collected as a function of EA:hexane ratio for an argon-cycled cell (left) and CO_2-cycled cell (right).

These same samples were subject to MALDI studies. Representative data are shown in Fig. 8. In these data, the sample is covered with a conductive matrix material and subjected to laser ablation and mass spectroscopy. These data show that the soluble portion of the SEI is significantly different with the introduction of CO_2. Specifically, we clearly observe the presence of large-molecular-weight PEO-type species (the repeat unit 44 AMU is the same as the MW of CO_2). These species are readily removed during DMC wash, which indicates that the DMC is too aggressive.

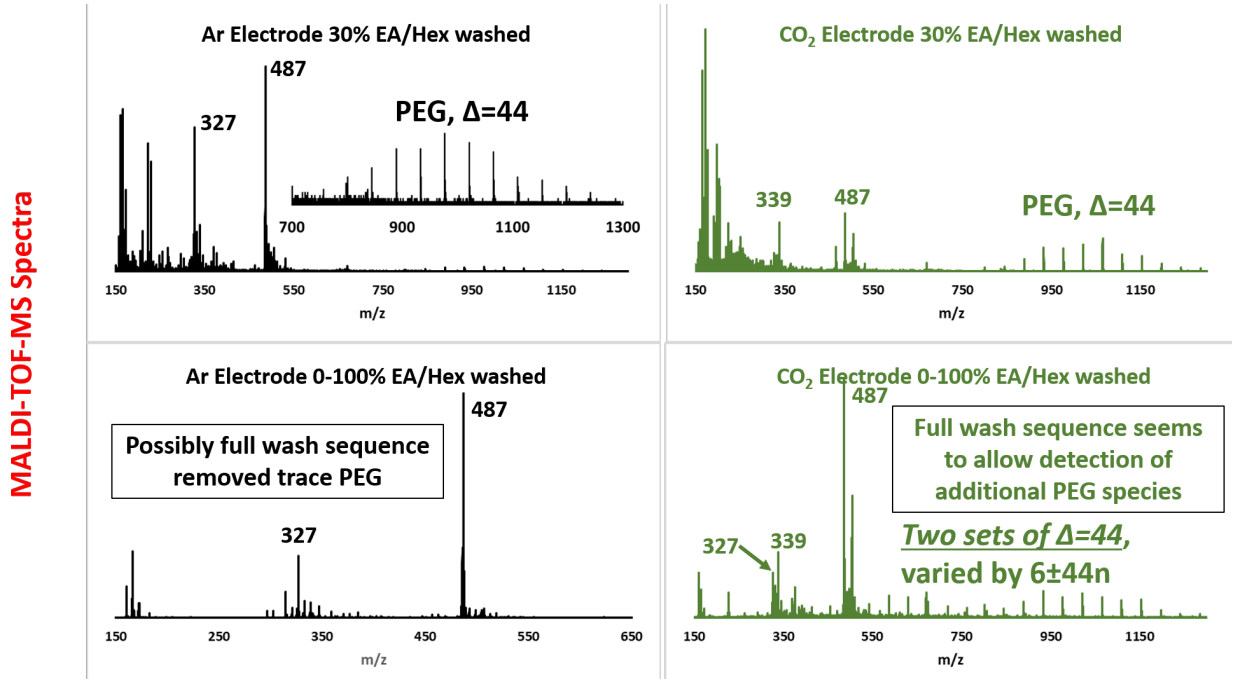

Figure 8. MALDI data measured for hexane-washed (bottom) and 70%-hexane-washed (top) electrodes cycled in argon (left) and CO_2 (right).

Further analysis of the unwashed electrodes was performed with $^{13}CO_2$-dosed cells. NMR data for these experiments are shown in Fig. 9. Although unclear about what are the data at this point, the clear differences in the NMR signals again indicate changes in SEI chemistry and electrolyte chemistry.

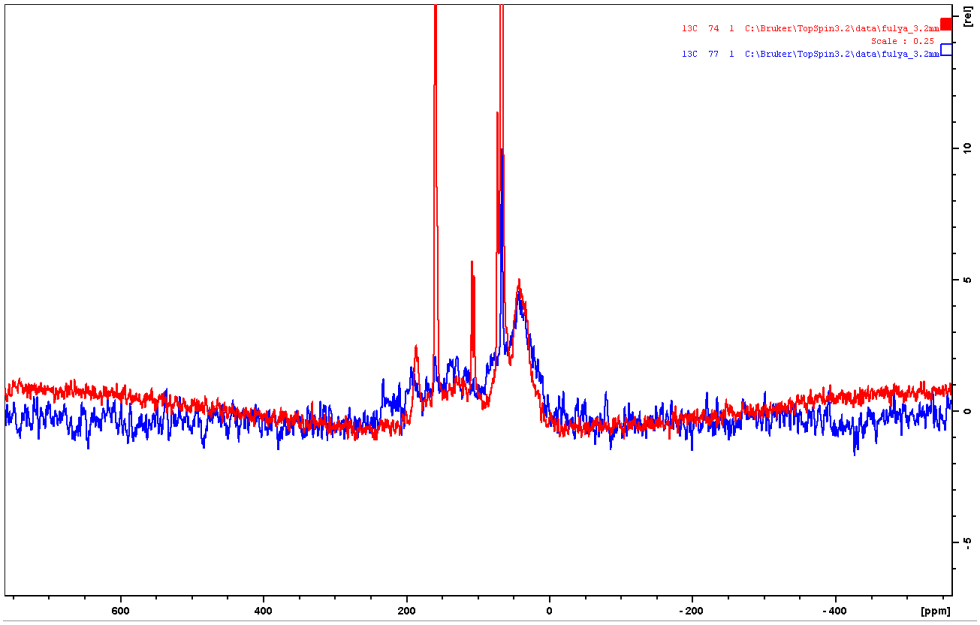

Figure 9. NMR data collected for cells with (red) and without (blue) CO_2.

Impact and Future Studies

The above data clearly demonstrate that CO_2 as an additive by itself does not solve capacity retention issues associated with silicon. However, this research leads to several fundamental questions, including:

1. What is the role of air? The data in Round 1 show a significant variation of SEI compared to Round 2 or Round 3. This would indicate that air has an effect on the SEI. The question is, why?

2. What happens in a full cell? The data above were collected in half-cell configurations. It is unclear if the Li metal reacts with the CO_2 or participates in a heretofore unidentified process. To answer this question, we are working on these same experiments using a $LiFePO_4$ composite slurry cathode. These experiments have begun and are ongoing.

3. Why do the $^{13}CO_2$ data look different than natural CO_2? The data collected on the $^{13}CO_2$ data look significantly different in terms of SEI chemistry. Note that the capacity retention is the same. We wonder, why? Our initial hypothesis is that the H_2O content in the two streams is different. We are working to explore this and control it better.

4. What is the role of water in SEI chemistry? As noted, our hypothesis is that water is playing a role in the SEI that is more significant than CO_2. This would be consistent if dry-ice sources bring condensed water to the cells. This is an area of future study.

5. What is the role of CO_2 solubility? We have explored our standard $LiPF_6$ ethylene carbonate:ethyl methyl carbonate electrolyte. Would the solubility be significantly different? Our measurements of gas solubility in this electrolyte reveal that we only dissolve about 0.2% CO_2.

6. How would these results change for cells with composite silicon anodes? We note that the full cell has a binder that may increase solubility of the CO_2 or change the activity of the CO_2 decomposition in an unidentified way.

All these questions are subject to future in-depth studies contingent on time and resources.

Conclusion

The data above conclusively show that the SEI chemistry changes with and without CO_2. However, this change does not significantly change the cyclability and capacity loss of the cells. More critically, a number of fundamental research directions have been identified that lead to greater understanding of the SEI chemistry.

References

n/a